
# Confronting physics of the early Universe with cosmological observations

by

**Joby P. K.**

Indian Institute of Astrophysics, Bangalore

A thesis submitted in partial fulfillment for the degree of Doctor of Philosophy to the

Department of Physics
University of Calicut
Calicut, Kerala

January 2019

# CERTIFICATE

This is to certify that the thesis titled **Confronting physics of the early Universe with cosmological observations** is a bonafide record of the work done by Joby P. K. under our joint supervision and that no part of it has been included previously for the award of any degree, either in this university or any other institution.

Supervisor
Dr. Pravabati Chingangbam,
Indian Institute of Astrophysics,
Bangalore.

Co-supervisor
Dr. Ravikumar C. D.,
Department of Physics,
University of Calicut, Kerala.

# CERTIFICATE

This is to certify that in the thesis titled **Confronting physics of the early Universe with cosmological observations** by Joby P. K., the corrections / suggestions from the adjudicators have been incorporated.

Supervisor
Dr. Pravabati Chingangbam,
Indian Institute of Astrophysics,
Bangalore.

Co-supervisor
Dr. Ravikumar C. D.,
Department of Physics,
University of Calicut, Kerala.

# DECLARATION

I hereby declare that the thesis titled **Confronting physics of the early Universe with cosmological observations** is an authentic record of research work carried out by me at the Indian Institute of Astrophysics under the supervision of Dr. Pravabati Chingangbam and Dr. Ravikumar C. D.. No part of this work has formed the basis for award of any other degree in any university or institution.

Joby P. K.
Indian Institute of Astrophysics
Bangalore 560 034
January 2019.

# ACKNOWLEDGEMENTS

I am extremely grateful to my PhD. supervisor and mentor, Dr. Pravabati Chingangbam, for her guidance and support. She taught me the fundamentals of cosmology and general relativity, which has formed the basis of my research. She has helped me in making the transition from being a student to a being a research scholar. She has helped me to develop an eye for detail. I thank her for being patient with me during my difficult times and being harsh when required. She has always encouraged me to come up with my own ideas and solutions to the problems I faced in my work, and given me the space and time to make mistakes and learn from them. This has played an important role in my growth as a researcher.

I would also like to thank my co-supervisor, Dr. Ravikumar C. D., for his valuable suggestions and also for helping me with the various administrative procedures at Calicut University.

I thank Dr. Subinoy Das, Dr. Tuhin Ghosh, Dr. Stephen Appleby and Dr. Changbom Park for their useful inputs and suggestions in our work. They have helped me in improving my understanding of the subject and also in practical aspects of our work related to coding.

I would like to thank Dr. Jayant Murthy, the Director of Indian Institute of Astrophysics (IIA), Dr. Aruna Goswami from the Board of Graduate Studies, IIA, Dr. G. C. Anupama, Dean, IIA, and all the administrative staff at IIA who have helped me with the various administrative procedures. I also thank Dr. K. M. Basheer, the Vice Chancellor, University of Calicut (UoC) and Dr. M. Nasser, Director of Research, UoC for approving the early submission of my thesis.

I thank my parents and my sisters who have played a vital role in my inclination towards science. Their continuous encouragement and support has made this journey possible.

I thank Vidhya for her suggestions and the useful discussions on physics and other topics. She has helped me with Linux and the various codes that we used during the course of this thesis. I also thank Akanksha and Priya for the many discussions which have helped me

gain valuable insights into the subject.

Last but not the least, I thank all my friends at IIA who played their part in this journey, academically and otherwise, making it a memorable experience.

# LIST OF PUBLICATIONS

## Refereed Journals

1. *Search for anomalous alignments of structures in PLANCK data using Minkowski Tensors*
   **Joby P. K.**, Pravabati Chingangbam, Tuhin Ghosh, Vidhya Ganesan, Ravikumar C. D., 2019, JCAP, 01, 009.

2. *Minkowski tensors in three dimensions - probing the anisotropy generated by redshift space distortion*
   Stephen Appleby, Pravabati Chingangbam, Changbom Park, K. P. Yogendran, **Joby P. K.**, 2018, ApJ, **863** 200.

3. *Tensor Minkowski Functionals for random fields on the sphere*
   Pravabati Chingangbam, K. P. Yogendran, **Joby P. K.** et al., 2017, JCAP, 12, 023.

4. *Constraint on noncommutative spacetime from PLANCK data*
   **Joby P. K.**, Pravabati Chingangbam and Subinoy Das, 2015, Phys. Rev. D 91, 083503.

# ABSTRACT

The Cosmic Microwave Background (CMB) is the oldest light in the Universe and gives us access to a picture of the Universe when it was only $\approx$ 300,000 years old. The CMB radiation consists of photons free streaming to us from the surface of last scattering. The existence of such radiation was predicted by Dicke and his group and was experimentally detected by Penzias and Wilson in 1965. The CMB gives us a window to study the fundmental laws of physics by observing the Universe on the largest scales. Precise measurements of the temperature and polarization fields of the CMB have allowed us to gain valuable physical insights about properties of our Universe. It is found that on length scales larger than $\approx$ 300 Mpc, our Universe is homogeneous and statistically isotropic. In the first part of our work, we test the fundamental assumption of SI and in the second part, we test the prediction of noncommutative spacetime.

The standard $\Lambda$CDM cosmological model is the most widely accpeted model of our Universe. The assumption of Statistical Isotropy (SI) is one of the important assumptions of the $\Lambda$CDM model and has been found to be consistent with most tests of isotropy using observations. However, there are many models which predict that our Universe is not isotropic and strong limits on the violation of SI can constrain these models. There isn't any *a priori* reason for the Universe to be statistically isotropic, and hence it is important to test this fundamental assumption which is one of the pillars of our understanding of the Universe. We have developed techniques to measure the isotropy of random fields on the sphere and in three dimensional flat space, and have used cosmological data to search for deviations from SI.

We use Minkowski Tensors (MTs), which carry information regarding the shape of closed curves, as a measure of isotropy. By choosing a suitable threshold to cut off a given field, we get closed curves which form the boundaries of the connected regions and holes. The isotropy and alignment of these closed curves provide information on the SI of the underlying field. MTs were previously defined for closed curves in flat spaces. However,

cosmological fields such as the CMB are defined on the sphere and thus the MTs can not be directly applied to these fields. We generalize the definition of MTs to closed curves on the sphere and provide a numerical method to estimate the MTs from pixelated maps. Further, we apply our technique to the CMB temperature data given by the *Planck* mission and find no signficant deviation from SI. We also apply our method to the beam convolved individual frequency CMB temperature maps given by *Planck* and find that they are all consistent with SI, except for the 30 GHz maps, which exhibit a mild level of anisotropy. We suspect that an inaccurate estimation of the instrument beam or residual noise at 30 GHz could be the primary reason for this mild discrepancy.

We have also used the MTs for three dimensional density fields to demonstrate a method to constrain the effect of Redshift Space Distortion (RSD). RSD is the modification of the apparent shape of galaxy clusters due to the peculiar velocity of the galaxies, which affects the measured redshift of the galaxy, making the Hubble's redshift-distance relation an inaccurate approximation. We compute the ensemble expectation values of the MTs for a 3D isotropic Gaussian field and develop a numerical and a semi-analytic method to estimate the MTs from a discretely sampled field. We apply our method to estimate the MTs from the isotropic fields and the anisotropic fields obtained by applying a linear RSD operator to the isotropic feilds. We find that RSD leads to a shift in the amplitude of the elements of the MTs and show that this shift can be used to obtain constraints on the linear RSD parameter.

In the last part of our work, we have tested spacetime noncommutativity, which is an essential prediction of string theory. Based on evidence from observations, it is believed that the early Universe went through a phase of accelerated expansion, known as Inflation. During this phase, very small regions of space were blown up to cosmological sizes in a very short amount of time. This allows us to search for spacetime noncommutativity, which is an effect relevant at the extremely small scales, by looking at cosmological fields such as the CMB. If our spacetime is noncommutative, then the form of the CMB angular power spectrum is modified and this effect can be used to constrain the energy scale of spacetime noncommutativity. First we estimate the effect of noncommutative spacetime on the CMB angular power spectrum using the publicly available package, CAMB, and show that *Planck* data is best suited to constrain the spacetime noncommutativity parameter. We then perform a Bayesian analysis of the *Planck* 2013 CMB temperature data and obtain a lower bound of $\approx 20$ TeV on the energy scale of spacetime noncommutativity. Our results, improve upon those of previous works by a factor of two.

Finally we summarize all the research work that was carried out as part of this thesis. We also discuss prospects for further research in the context of future CMB experiments having higher resolutions than *Planck* and the application of MTs for probing the SI of the CMB polarization fields as well as the CMB foregrounds.

# NOTATIONS AND ABBREVIATIONS

| | |
|---|---|
| CMB | Cosmic Microwave Background |
| CDM | Cold Dark Matter |
| WIMPS | Weakly Interacting Matter Particles |
| COBE | COsmic Background Observer |
| FIRAS | Far InfraRed Absolute Spectrophotometer |
| DIRBE | Diffuse InfraRed Background Experiment |
| WMAP | Wilkinson Microwave Anisotropy Probe |
| LFI | Low Frequency Instrument |
| HFI | High Frequency Instrument |
| SI | Statistical Isotropy |
| LSS | Large Scale Structure |
| BiPOSH | BiPOlar Spherical Harmonics |
| MFs | scalar Minkowski Functionals |
| MTs | Minkowski Tensors |
| BAO | Baryon Acoustic Oscillations |
| HEALPIX | Hierarchical Equal Area and iso-Latitude Pixelation |
| CAMB | Code for Anisotropies in the Microwave Background |
| PDF | Probability Distribution Function |
| FWHM | Full Width at Half Maximum |
| $N_{side}$ | HEALPIX resolution parameter |
| FFP | Full Focal Plane |
| GHz | Giga Hertz |
| JCAP | Journal of Cosmology and Astroparticle Physics |
| ApJ | Astrophysical Journal |
| Astron. Astrophys. | Astronomy and Astrophysics |

| | |
|---|---|
| MNRAS | Monthly Notices of the Royal Astronomical Society |
| RSD | Redshift Space Distortion |
| **Det** | Determinant |
| RMS | Root Mean Square |
| MCMC | Markov Chain Monte Carlo |
| TeV | Tera Electron Volts |

# LIST OF FIGURES

# CONTENTS

# 1

# INTRODUCTION

## 1.1 Cosmic Microwave Background

The Cosmic Microwave Background (CMB) is a background black body radiation which is observed in all directions of the sky. It was accidentally discovered by Arno Penzias and Robert Wilson while they were making a radio receiver and found that it was detecting noise [1]. Later, they realized that the noise was detected in every direction of the sky with the same intensity. Around the same time, the existence of CMB was also predicted by a research group led by Robert Dicke [2]. The CMB provided strong evidence for the Big Bang cosmological model which states that the Universe was initially hot and dense and later expanded and cooled down to the state that it is in today. The CMB is electromagnetic radiation which peaks in the microwave region today and gives us the earliest "picture" of the Universe that we have access to. For their discovery of the CMB, Penzias and Wilson received the Nobel Prize for Physics in 1978.

The CMB is relic radiation from the early stages of evolution of the Universe and its discovery has lead to many important advancements in the field of cosmology. Studies of the CMB temperature and polarization have helped us to deepen our understanding of the Universe. Today we have many competing models of the Universe which make different predictions for the properties of the CMB. Precise observations of the CMB provide us with a way to test these models. It is widely believed that our Universe in its early stages went through a phase of accelerated expansion, known as Inflation [3–7]. This concept and its predictions for the CMB are discussed in Section 1.4. Observations of the CMB sky have given support to this idea and it has contributed to the development of the standard $\Lambda$CDM model of cosmology.

Today the study of CMB observations have found applications in other fields including particle physics. The CMB provides one of the strongest experimental evidences for physics beyond the standard model. It tells us that a strong majority of the energy density in our Universe consists of mysterious Dark Energy which is believed to drive the late time accelerated expansion of the Universe, and Dark Matter which is invisible to us and forms $\approx 80\%$ of the mass in the Universe. The analysis of CMB data have given us constraints on the masses and number of species of neutrinos as well as constraints on dark matter candidates such as axions and Weakly Interacting Massive Particles (WIMPs). The CMB has a huge contribution in the development of our current understanding of the Universe. In the following section, we discuss the various experiments which were designed to measure the CMB temperature and polarization fields.

## 1.2 Measurements

The main observables of the CMB radiation are the temperature and polarization of the photons. The polarization field can be divided into two parts, a curl free part and a gradient free part. The curl free part is referred to as the $E$ mode while the gradient free part is referred to as the $B$ mode of CMB polarization. In this section, we describe some of the major experiments which were designed to measure the CMB observables.

### 1.2.1 COBE

COBE stands for COsmic Background Explorer and it was a satellite launched in 1989 to make measurements of the CMB radiation. This mission carried three instruments, the Differential Microwave Radiometer (DMR) for measuring the anisotropies in the CMB temperature, the Far-InfraRed Absolute Spectrophotometer (FIRAS) for measuring the spectrum of the CMB, and the Diffuse InfraRed Background Experiment (DIRBE) to map the emission due to dust. COBE was placed in a circular Sun-synchronous orbit at an altitude of 900 km, given the requirements of full sky coverage and maintenance of thermal stability of the instruments. COBE mapped the CMB sky for four years from 1989 to 1993.

This mission carried out full sky observations of the CMB in fourteen frequency channels. It is also the first experiment to make precise measurements of the CMB frequency spectrum. FIRAS measured the CMB spectrum in the frequency range 1 to 100 $\text{cm}^{-1}$ and found that it was a black body spectrum [8]. This confirmed the prediction of the hot Big Bang model that the Universe in its early stages was in thermal equilibrium. The fluctuations in the CMB temperature were detected for the first time and measured with a

sensitivity of the order of $10^{-5}$ and an angular resolution of $7^{\circ}$ [9]. The diffuse infrared sky emission was mapped by the DIRBE instrument [10]. George Smoot and John Mather were the principle investigators of the COBE mission and received the Nobel Prize for Physics in 2006.

### 1.2.2 WMAP

COBE experimentally confirmed the prediction of the black body spectrum of the CMB photons and also detected the CMB temperature anisotropies. Following this development, there was a need to make high precision measurements of the CMB temperature and polarization anisotropies for constraining models of cosmology. In this light. the Wilkinson Microwave Anisotropy Probe (WMAP) was designed to make precise measurements of the CMB anisotropies with error margins that would be well understood. WMAP made observations of the CMB in five frequency bands to minimize the systematic errors associated with particular radiometers, and over a period of nine years to minimize the time dependent systematic erros. It was placed in the Sun-Earth $L_2$ Lagrangian point and conducted its survey from 2001 to 2010.

WMAP made a full sky map of the CMB anisotropies with a resolution of 13 arcminutes by combining observations at multiple frequencies. The map of the CMB sky created by WMAP was found to be statistically consistent with that created by COBE despite the differences in hardware and orbits. The WMAP data suggested that our Universe is best described by the standard $\Lambda$CDM model with six parameters [11]. While it found a strong alignment between the quadrupole and octupole components of the CMB sky [12], there was no convincing explanation for this alignment. The nine years data was used to estimate the values of the cosmological parameters with precisions of up to 1% and found no significant deviations from the $\Lambda$CDM cosmological model.

### 1.2.3 *Planck*

The *Planck* mission was launched in 2009 with the goal of extracting all the information that could possibly be gained from the CMB temperature fluctuations. This would give the most accurate to date estimations of the age of the Universe, amount of baryonic matter, dark matter and dark energy in the Universe. It was also aimed to catalogue the galaxy clusters with the help of the Sunyaev-Zel'dovich effect and trace the distribution of dark matter with the help of gravitational lensing. Additionally, it also measured with high precision, the foreground emissions from sources such as thermal dust and synchrotron

radiation in order to facilitate better cleaning of the CMB maps.

The instruments on board the *Planck* mission had higher sensitivity and angular resolution as compared to its predecessors and were expected to give the most precise measurements of the CMB. *Planck* observed the CMB sky in nine frequency channels ranging from 30 GHz to 857 GHz as compared to five channels of WMAP. The Low Frequency Instrument (LFI) made observations in the frequency range 30 GHz to 70 GHz, while the High Frequency Instrument (HFI) made observations in the frequency range 100 GHz to 857 GHz. *Planck* produced CMB sky maps with significantly improved angular resolution of up to 5 arcminutes [13] as compared to 13 arcminutes of WMAP. As a result, these maps could probe multipoles up to 2500 while WMAP could only probe multipoles up to 850. The data from this mission was able to estimate the value of the Hubble parameter today with uncertainties $\approx 1\%$ and this is tension with local measurements of the Hubble parameter. This result is one of the biggest anomalies that are yet to be resolved in modern cosmology.

## 1.3 Characteristics of CMB

The CMB radiation is observed to be extremely isotropic. The measured brightness temperature of the CMB photons coming from different directions in the sky differs only at the level of one part in $10^5$ [9]. The frequency spectrum of the CMB is a blackbody spectrum having a temperature of $\approx 2.7$ Kelvin. Studies of the CMB temperature fluctuations reveal that they have a Gaussian probability distribution function with a standard deviation of $\approx 10^{-4}$ Kelvin. For a Gaussian random field, all information content of the field is encoded in its power spectrum. The CMB fields are defined on the sphere and so we analyze its angular power spectrum to extract information. For ease of calculation, first the mean temperature is subtracted from the map to give a field of temperature fluctuations. Next, the temperature fluctuations field is decomposed into spherical harmonics as,

$$\Delta T(\theta, \phi) = \sum_{\ell=0}^{\ell_{max}} \sum_{m=-\ell}^{+\ell} a_{\ell m}\, Y_{\ell m}(\theta, \phi) \tag{1.1}$$

where $\Delta T(\theta, \phi)$ denotes the temperature fluctuation in the direction defined by the spherical coordinates $\theta$ and $\phi$, $Y_{\ell m}$ are the spherical harmonics and $a_{\ell m}$ are the respective coefficients. If the Universe is isotropic, then the angular power spectrum of $\Delta T$ can be given as,

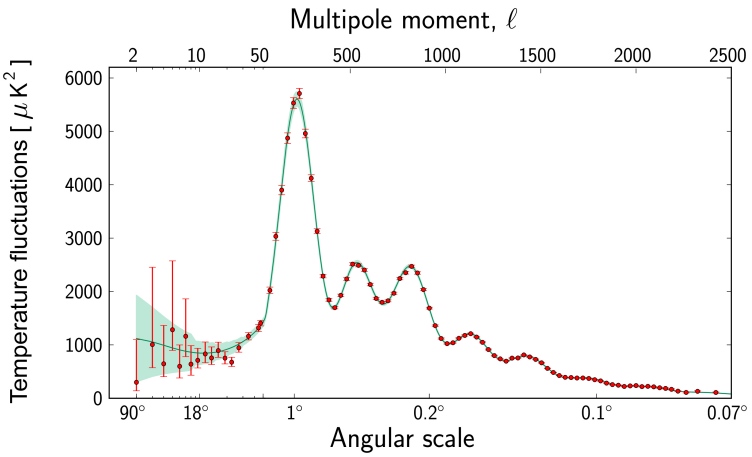


Figure 1.1: The CMB temperature fluctuations angular power spectrum based on full sky observations by *Planck* [15].

$$\mathcal{C}_\ell \equiv \frac{1}{2\ell+1} \sum_{m=-\ell}^{+\ell} |a_{\ell m}|^2 \tag{1.2}$$

where $\mathcal{C}_\ell$ denotes the power in the multipole $\ell$. Fig. 1.1 displays the angular power spectrum of the CMB temperature anisotropies as measured by *Planck*.

The observed features such as peaks, and drop in power at high $\ell$ in the angular power spectrum carry information on the physical processes and the state of the Universe when the CMB photons were emitted. Before the epoch of last scattering, the Universe could be described as a photon-baryon plasma under the effect of two main competing forces: the gravitational force pulling the contents together and the radiation pressure generating an outward force. This resulted in periodic fluctuations in the baryon density field which leads to the acoustic seen peaks in the CMB angular power spectrum. As seen in Fig. 1.1, the first acoustic peak in the CMB power spectrum is seen at $\ell \approx 220$, which corresponds to an angular scale of $\approx 0.82°$. As the photons began to free stream after the last scattering, their diffusion from hot regions to cold regions reduced the differences in temperatures between the different regions. This is known as *Silk Damping* and explains the observed decline in power at large multipoles in the CMB power spectrum [14].

## 1.4 Inflation

The hot big bang model of the Universe has been very successful at explaining astronomical observations. However, there are a few issues with the standard big bang model which need to be addressed. One of the problems is the observed homogeneity in the temperature measurements of the CMB [4]. CMB radiation observed in opposite directions in the sky, originate in regions which were at the time of emission of CMB, further away than the distance that light could have travelled in the age of the Universe. This means that when the CMB was emitted, these regions could not have been in causal contact. However, the measured CMB temperature is about 2.7 Kelvin for all directions in the sky, with fluctuations of the order of $10^{-5}$, suggesting that the Universe was in thermal equilibrium at that time. This leaves us with the question as to how regions which were not in causal contact, could have been in thermal equilibrium. This is known as the horizon problem. Another issue is the observed flatness of the Universe. The required density of the Universe to halt the expansion of the Universe, but not to lead to a recollapse is called the critical density. It is found that the density of our Universe today is extremely close to the critical density required for a flat Universe. This means that in the very early Universe, the density would have differed from the critical density at only one part in $10^{57}$ [4]. It is a problem then to explain such a high level of fine tuning of density in the early Universe and is known as the flatness problem.

To address these and some other problems in the big bang model, Alan Guth came up with the idea of cosmic inflation. In this model, he proposed that after the big bang, the Universe went through a phase of exponential expansion [4]. It provides an elegant solution to the horizon and flatness problems. Before inflation, the Universe was consisted of a small dense region which was in causal contact and thermal equilibrium. Regions that are widely separated today were initially very close to each other prior to inflation. This explains the observed isotropy in the CMB temperature sky. During inflation, the Universe expanded by an order of about $10^{28}$ in a fraction of a second and this rapid expansion caused the space to become more flat irrespective of the initial density of the Universe, thus solving the flatness problem.

The particle associated with the field that drives inflation is called the inflaton. The quantum fluctuations of the inflaton field gave rise to the initial density perturbations in the Universe. The density perturbations in turn curved the spacetime around them and gave rise to the primordial perturbations in the metric describing our spacetime. These

perturbations are often referred to as the primordial curvature perturbations. Most inflation models predict that the primordial curvature perturbations have a nearly scale invariant power spectrum of the form,

$$P(k) = A_s \left(\frac{k}{k_0}\right)^{n_s - 1}, \tag{1.3}$$

where, $A_S$ is the amplitude of scalar perturbations, $n_s$ is the spectral index of scalar perturbations and $k_0$ is the pivot scale.

These initial density perturbations gave rise to the fluctuations in the CMB temperature sky that we observe today. After their emission, the CMB photons undergo physical processes such as redshift due to cosmic expansion, gravitational redshift and lensing due to the distribution of matter and scattering off free electrons, before reaching us, the observers. The initial density perturbations also evolve under the effect of gravity and cosmic expansion to produce the matter density distribution in our Universe today. Observing the CMB temperature fluctuations and polarization fields and the matter density distribution fields today gives us an opportunity to test the various models of inflation.

## 1.5 Last scattering

Post inflation, the inflaton field is believed to have decayed into the standard model particles. The Universe at this point could be described as a hot plasma of electrons and protons. The photons would travel a short distance before scattering off the free electrons. This plasma was opaque and the mean free path of the photons was very small. Protons and electrons would combine to form neutral hydrogen atoms but high energy photons would ionize the newly formed atoms to give free protons and electrons. As the Universe continued to expand, it cooled down and the density of matter and radiation decreased. As the temperature of the Universe decreased, the energy of the photons also decreased and there came a point when the photon energies were not high enough to ionize the neutral atoms. Since then, stable hydrogen atoms started forming and the free electrons available to scatter the photons became scarce. As a result, the photons started to free stream and this epoch is called the epoch of last scattering. The epoch of last scattering is believed to have occurred at a redshift of about 1100 [16, 17]. Today we observe this radiation emitted at the time of last scattering and it is called the cosmic microwave background radiation. The CMB photons that we receive today originate from a spherical surface in the sky, with us at the center, and a radius equivalent to the distance travelled by light in a time interval equal to the age of the Universe. This surface is known as the surface of last scattering.

## 1.6 Summary

The work carried out for this thesis, focuses on the testing of various fundamental principles of physics against cosmological observations. This chapter is aimed a providing an introduction to the subject with a brief account of some key concepts. For the most part of my work, I have used observations of the CMB temperature fluctuations field. In this chapter we have discussed the prediction and discovery of the CMB radiation. We have also discussed the importance of CMB observations in modern cosmology in the context of testing the various models of our Universe, and their relevance to other areas of physics such as particle physics. We have also presented a review of some of the experiments which were aimed at making measurements of the CMB temperature and polarization fields. Of these experiments, *Planck* provides the most precise measurements of the CMB, and we have used *Planck* CMB temperature data in our work. We have also reviewed some of the characteristics of the observed CMB radiation. The CMB temperature is found to have a Gaussian distribution and is extremely isotropic across the sky with small fluctuations of the order of $10^{-5}$. The angular power spectrum of the CMB contains features such as acoustic peaks and these features provide useful information about our Universe such as the density of matter and baryons.

We have also reviewed some of the problems with the standard hot big bang model and explained how cosmic inflation resolves these issues. The quantum fluctuations of the inflaton field lead to the anisotropies in the CMB temperature that we observe today. Further, these quantum fluctuations also give rise to the distribution of matter in our Universe. We have also discussed the epoch of last scattering after which the Universe became transparent and photons free streamed to us as the CMB radiation. The next chapter contains a discussion on the usefulness of the CMB in regard to cosmology. It also contains the motivation for our work and a brief account of the research problems that are part of this thesis.

# 2

# MOTIVATION, QUESTIONS AND METHODOLOGY

## 2.1 Physical insights from the CMB

The Universe cooled down as it expanded and there came a point when the photons got decoupled from matter and this epoch is know as the last scattering. The photons from last scattering practically free streamed and contain information about the state of the Universe at the time of last scattering. These photons give us the earliest picture of the Universe that is accessible to us for observations and are called the Cosmic Microwave Background (CMB) radiation. The CMB can give us useful insights on the physics of the early Universe. Each inflation model predicts certain features in the CMB power spectrum and hence measurements of the CMB power spectrum can constrain these models. Inflation leads to tiny regions in the early Universe to expand to cosmological sizes in a very short time and this gives us an opportunity to constrain physics at the small scales with CMB observations.

The CMB radiation can also be used to probe some physical processes that occur post the epoch of last scattering. On their way from the last scattering surface to the observer, the CMB photons interact with the different constituents of the Universe and undergo processes such as gravitational lensing and integrated Sachs-Wolfe effect. Information about these processes is then encoded in the CMB photons which we observe today and can be extracted with suitable analysis of the data. Thus the CMB can give us useful information about the physics of our Universe, both in its early and late stages.

## 2.2 Research problem

The main objective of my research has been to study fundamental physics and apply it to the early Universe and test them using observational data. In my PhD work, I have mainly looked at two aspects of the fundamental physics of the early Universe: statistical isotropy (SI), which is assumed by many models, and the noncommutativity of spacetime as predicted by some quantum theories of gravity.

### 2.2.1 Statistical isotropy

One of the important assumptions of the widely accepted $\Lambda$CDM cosmological model is that our Universe is statistically isotropic. However, there are many models which suggest that the early Universe was not statistically isotropic [18–27]. It is important to test this assumption in order to improve our understanding of the Universe. Tests of SI are usually based on cosmological data such as the CMB and the Large Scale Structure (LSS). In the literature, methods such as the BiPolar Spherical Harmonics (BiPosh) [28] and the power tensor [29] have been used to test the SI of CMB fields.

The tensor generalizations of the usual scalar Minkowski Functionals (MFs) are called Minkowski Tensors (MTs). MTs carry shape information which can be used to test the SI of fields by estimating the "average" shape of the structures (connected regions and holes) in the fields. Chapter 3 contains a brief review of the MT definitions and an explanation on how we can extract shape information from them. The definitions of the MTs contain the position vector which is not well defined for the general curved manifold and hence, they can not be directly applied to CMB fields which are defined on the sphere. In [30], the authors make stereographic projections of the CMB temperature fluctuations and polarization fields on to a plane and test the SI of the projected CMB fields. They found a $\approx 4$-$\sigma$ deviation from SI in the CMB $E$ mode data.

Stereographic projection preserves angles but can scale the sizes of structures in the field and hence it is important to test the above mentioned result by computing MTs for the CMB fields directly on the sphere. We achieve this goal by rewriting the definitions of the MTs in terms of the tangent vector to the curve. The tangent vector is well defined for every smooth manifold and so the MTs can be applied even to curved spaces. This work and its applications to the *Planck* 2015 CMB data has been discussed in detail in Chapter 4. We have also investigated the effect of redshift space distortion on the distribution of matter and how it is captured by the MTs in three dimensions. In Chapter 5, we have discussed a

method to constrain the linear redshift space distortion parameter using MTs for the three dimensional distribution of matter in our Universe.

### 2.2.2 Spacetime noncommutativity

Many quantum theories of gravity predict that our spacetime is noncommutative. If it is true, then it means that for an observed event, the order in which the spatial and time coordinates are measured becomes important. This is not observed in classical physics and is an effect that would be relevant at extremely small length scales, comparable to the Planck length scale. Since inflation blows up tiny regions of space to cosmological sizes and this encodes information about small scale physics in the CMB, it gives us an opportunity to study noncommutativity of spacetime by analyzing the CMB fields. In the context of the CMB, the noncommutativity of spacetime modifies the form of the CMB angular power spectra and by searching for this effect in the CMB data, we can constrain the length scale at which spacetime noncommutativity becomes relvant.

Spacetime noncommutativity can be represented by the following relations [18, 19].

$$[\hat{x}^{\mu}, \hat{x}^{\nu}] = i\theta^{\mu\nu} \tag{2.1}$$

where $\hat{x}^{\mu}$ are the coordinate operators. We study the simplest case of noncommutative spacetime where the tensor $\theta^{\mu\nu}$ is considered to have only one independent element and we call it $\theta$. If this model is correct then it would affect the initial quantum fluctuations of the inflaton field and modify the primordial scalar power spectrum. As a consequence, the power spectrum of the CMB temperature flucuations and polarization would also get modified. In the simplest case, taking $\theta$ as a constant, the modified expression for the CMB angular power spectrum of temperature fluctuations can be given as [18],

$$C_{\ell}^{\theta} = \int dk k^2 \left|\Delta_{\ell}(k)\right|^2 P(k) i_0(\alpha k) \tag{2.2}$$

where $P(k)$ is the usual primordial scalar power spectrum in commutative spacetime. $|\Delta_{\ell}(k)|$ are the CMB transfer functions, $\alpha = H\theta$ where $H$ is the Hubble parameter at the end of inflation and $i_0(x) = \frac{\sinh(x)}{x}$. We can test the presence of this effect in the observations of the CMB temperature fluctuations. Spacetime noncommutativity has a similar effect on the angular power spectrum of CMB polarization and hence measurements of CMB polarization can also provide constraints on spacetime noncommutativity. This work is discussed in detail in Chapter 6.

## 2.3 Observational data

Throughout this work, we have tested assumptions of fundamental physics against CMB observations. In Chapter 6, we have used the CMB temperature fluctuations data given as part of the *Planck* 2013 [31] data release to constrain the spacetime noncommutativity parameter. Additionally, we also obtain constraints on the noncommutativity of spacetime for combinations of CMB temperature fluctuations data from *Planck* and Baryon Acoustic Oscillations (BAO) data from SDSS [32, 33] and 6DFGS [34] and CMB polarization data from BICEP2 BICEP2 [35]. *Planck* has higher angular resolution than WMAP and higher precision compared to ACBAR and CBI and hence our constraints are expected to be significantly tighter than previous work which used WMAP, ACBAR and CBI data.

In Chapter 4, we have used pure CMB simulations generated by the SYNFAST routine [36, 37] to test the effect of masking, smoothing and pixel size on the computation of MTs for CMB fields. We have also used the foreground and noise maps given as part of the *Planck* 2015 data release [38] to study the behaviour of the alignment parameter $\alpha$ in toy models which violate SI. We have used the CMB temperature fluctuations map provided by the SMICA pipeline [39, 40], along with FFP8.1 SMICA simulations which include residual foreground and noise, to look for deviations from SI in the CMB temperature anisotropies. We have also used the beam convolved CMB temperature maps at individual frequencies cleaned by the Commander [41, 42], NILC [43, 44], SEVEM [45, 46] and SMICA [39, 40] cleaning methods along with the FFP9 simulations to probe for violation of SI.

## 2.4 Software packages: HEALPIX, CAMB and COSMOMC

We have used three publicly available software packages for testing our methods on simulations as well as for performing the analysis of observed data. In this section we discuss the software packages that were used during the course of this work.

### 2.4.1 HEALPIX

HEALPIX stands for Hierarchical Equal Area and iso-Latitude Pixelation of the sphere [36, 37]. As the name suggests, it was designed to divide the surface of a sphere into pixels having the same surface area. These pixels can be easily divided further into smaller pixels of equal area corresponding to a higher resolution map. In HEALPIX terms, the resolution

of a given map is represented by the parameter called "Nside". For a map with a resolution parameter of Nside, the number of pixels is given by $12\times\text{Nside}^2$. Additionally, this package contains several routines which are extremely useful for the analysis of pixelated fields on the sphere. The alm_tools module contains subroutines for the decomposition of a field defined on the sphere, into spherical harmonics and vice versa. It also contains subroutines for computing the derivatives of the field in spherical coordinates as well as smoothing the field with a Gaussian kernel of a specified beam width. The synfast subroutine generates a realization of the CMB sky for a specified seed value. These subroutines have been extensively used during the course of this work for the purpose of generating simulations of the CMB sky and the analysis of both the data and the simulations.

### 2.4.2 CAMB

CAMB is an acronym for Code for Anisotropies in the Microwave Background [47, 48], developed by Antony Lewis and Anthony Challinor. It is an open source code that numerically solves the Boltzmann equation for the Universe to compute the CMB and matter power spectra, as well as the CMB transfer functions. Provided an input model of the Universe, CAMB computes the CMB temperature fluctuations, polarization and lensing power spectra for a specified redshift. We have used CAMB in the work described in Chapter 4 to compute the CMB power spectra that was used to generate the CMB sky simulations, and in the work described in Chapter 6 to test the effect of spacetime noncommutativity on the CMB power spectra. This package is also provided as part of the COSMOMC package which is dicussed below.

### 2.4.3 COSMOMC

COSMOMC is a publicly available Fortran code for performing cosmological parameter estimation by doing a Markov Chain Monte Carlo analysis of the data [48, 49]. It was developed by Antony Lewis, who is also the author of CAMB. It uses the Bayes theorem which provides a way to compute the conditional probability of a model being the correct description of the Universe for a set of observations. Given a model with a certain number of free parameters and a set of observations, this package computes the best fit parameter values and also the 1-$\sigma$ and 2-$\sigma$ confidence regions. In our search for the signatures of noncommutative spacetime in the CMB datasets, we use COSMOMC to analyse the *Planck*, BICEP2 and SDSS data to establish constraints on the energy scale of spacetime noncommutativity.

## 2.5 Summary

This chapter gives the motivation for the work which was carried out for this thesis. We revisit some of the basics of CMB physics and mention the physical insights that we can gain from studying the CMB. This includes information on the physics of the early Universe, from constraining models of inflation to the laws of physics that apply at the small scales. Further, by studying cosmological fields such as the CMB and LSS, we can also learn about the distribution of matter in our Universe today.

We have discussed here the research problems that we have investigated as part of my PhD work, mainly the prediction of noncommutative spacetime and the fundamental assumption that our Universe is statistically isotropic. We have given the relevance of these studies to physics and have also mentioned the various observational datasets that were used. For testing the prediction of noncommutative spacetime, we have mainly used CMB data from *Planck* and BICEP2, while for probing SI we have used CMB temperature flucuations data from *Planck*.

Finally we introduce the software packages that have been used for these analyses. The HEALPIX package provides a method to divide a spherical surface into equal area pixels. It also comes with useful modules for decomposition of a field into spherical harmonics and vice versa and generating simulated CMB sky maps of a specified resolution. CAMB solves the Boltzmann equations for a given set of input parameters to estimate the CMB and matter power spectra and the CMB transfer functions. COSMOMC is a software package for cosmological parameter estimation from a combination of observed datasets.

# 3

# MORPHOLOGY OF RANDOM FIELDS IN FLAT 2D SPACE

## 3.1 Introduction

We test the principle of Statistical Isotropy (SI), which is a fundamental assumption of the standard ΛCDM cosmological model, using CMB data. For this purpose, we treat the cosmological fields as random fields on two or three dimensional spaces. Statistical analysis of these fields give us information on the broad features of the Universe, which is how we develop our understanding of the Universe. In two dimensions, the Cosmic Microwave Background (CMB) temperature and polarization fields [1,9,50] are among the most important cosmological fields. The theory of Gaussian random fields on the sphere, relevant to the CMB fields, was developed by Bond and Efstathiou [51]. This was based on the theory of excursion sets of random fields developed by Adler [52]. To test the SI of these CMB fields, we use mathematical quantities called Minkowski Tensors (MTs) which carry information regarding the shape of closed curves. In this chapter, we review the definitions of the scalar Minkowski Functionals (MFs), their tensor generalizations MTs, in two dimensions, and discuss how the MTs can be used to search for violations of SI in the CMB fields.

Scalar Minkowski Functionals have been widely used in the study of cosmological fields [53–60]. MFs contain correlations of arbitrary order and are defined on real space. MFs have been used to search for primordial non-Gaussianity [60–65], effect of residual foreground in CMB data [66] and effect of lensing on CMB fields [67, 68]. However, MFs are not sensitive to morphological information such as the shape and alignment of

structures. Related quantites like the count of hot spots and cold spots [69–71] and extrema counts [72] have also been applied to cosmological fields.

Minkowski Tensors are tensor generalizations of the scalar MFs and have been defined for flat two and three dimensional spaces [73–78]. In this chapter we will briefly review the scalar MFs and MTs in flat 2D space and also the advantages of using MTs over MFs. MTs can be classified into translation invariant and translation covariant ones. One of the rank two translation invariant MTs contains information about the shapes of connected regions and holes in random fields and their relative spatial alignment. Ganesan and Chingangbam [30] applied this method to the CMB temperature fluctuations and $E$ mode of polarization data given in *Planck* 2015 release [13] and found that the $E$ mode data exhibit significant level of alignment. We expect that an analysis of the full *Planck* data would shed more light on the physical origin of this alignment.

This chapter is organized as follows, we first review the definitions of scalar MFs and MTs in flat 2D space and focus on the translation invariant rank 2 MTs . Next, we describe how to obtain connected regions and holes from a random field. The boundaries of these connected regions and holes form closed curves that MT statistics can be applied to. We discuss how information regarding the intrinsic isotropy of structures in a random field and their relative alignment are contained in one of the MTs. We explain how the MTs can used to study the statistical isotropy of random fields. Applications of MTs to CMB data is covered in chapter 4.

## 3.2 Scalar Minkowski Functionals

For a closed curve in flat 2D space as shown in Fig. 3.1, we can define three MFs, the area fraction, the contour length and the genus. Here we shall describe these quantities along with their mathematical expressions.

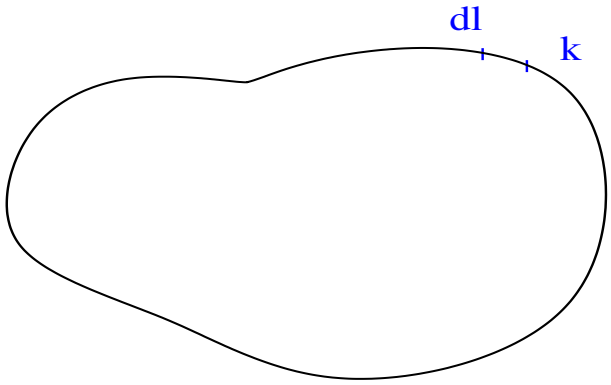


Figure 3.1: A closed curve in flat 2D space. d$l$ is the line element on the curve and $\kappa$ denotes the curvature at each point on the curve.

1. Area fraction: It is the ratio of the area enclosed by the closed curve to the total area over which the field is defined. We shall denote it by $V_0$. Mathematically, it can be given as,

$$V_0 \equiv \frac{1}{A} \int \mathrm{d}a$$

where, $A$ is the total area over which the field is defined and d$a$ is the area element in the region enclosed by the curve.

2. Contour length: It is the perimeter of the closed curve and we denote it by $V_1$. It can be written as,

$$V_1 \equiv \frac{1}{4} \int_C \mathrm{d}l$$

where, $C$ denotes the closed curve and d$l$ is the line element on C.

3. Genus: For a set of closed curves, the genus represents the number of closed curves. Closed curves that form boundaries of hotspots are counted as +1, while those that form boundaries of cold spots are counted as -1. A description of hotspots and cold spots in random fields defined on flat 2D space is given in section 3.4. The genus for a set of closed curves is denoted as $V_2$ and is given by,

$$V_2 \equiv \frac{1}{2\pi} \int_C \kappa \, \mathrm{d}l$$

where, $\kappa$ is the curvature for each point on the curves.

MF statistics can provide useful insights into the nature of the field. However, they do no contain information on the shapes and alignment of the structures in the field. To get shape and alignment information, we use Minkowski Tensors.

## 3.3 Minkowski Tensors in flat 2D space

Scalar MFs are a subset of the more general Minkowski Tensors. In this section we review the definitions of MTs of rank (*m*,*n*) on flat 2D space. We will then focus on the rank two translation invariant MTs and discuss how they provide shape information.

For a closed curve *C*, we denote the position vector of a point on the curve by $\vec{r}$, the unit normal to the curve by $\hat{n}$ and the local curvature of the curve at the point by $\kappa$. MTs for the curve are defined as follows (see [77]):

$$\begin{aligned} W_0^{m,0} &= \int_C \vec{r}^{\,m} \mathrm{d}a \\ W_1^{m,n} &= \tfrac{1}{2} \int_C \vec{r}^{\,m} \otimes \hat{n}^{\,n} \mathrm{d}s \\ W_2^{m,n} &= \tfrac{1}{2} \int_C \vec{r}^{\,m} \otimes \hat{n}^{\,n} \kappa \mathrm{d}s, \end{aligned} \tag{3.1}$$

where, $C$ denotes the closed curve, $da$ denotes the area element in the region enclosed by the closed curve and $ds$ is the line element on the curve. $\otimes$ denotes a tensor product of two vectors and is defined as the symmetric product $\left(\vec{A} \otimes \vec{B}\right)_{ij} = \frac{1}{2}\left(A_i B_j + A_j B_i\right)$. $\vec{r}^{m}$ denotes the $m$-fold tensor product of $\vec{r}$ and similarly for $\hat{n}$.

The usual scalar MFs are the rank-0 MTs. The rank-1 MTs are translation covariant. MTs of rank-2 can be classified as translation covariant and translation invariant ones. $W_1^{1,1}$, $W_1^{0,2}$, $W_2^{1,1}$ and $W_2^{0,2}$ are the translation invariant MTs. From these MTs, $W_1^{0,2}$ and $W_2^{1,1}$ are dependent on each other. We choose the linearly independent translation invariant MTs to be

$$\begin{aligned} W_1^{1,1} &= \tfrac{1}{2} \int_C \vec{r} \otimes \hat{n} ds \\ W_2^{1,1} &= \tfrac{1}{2} \int_C \vec{r} \otimes \hat{n} ds \\ W_2^{0,2} &= \tfrac{1}{2} \int_C \hat{n} \otimes \hat{n} ds \end{aligned} \tag{3.2}$$

These MTs are related to the scalar MFs as

$$\begin{aligned} V_0 \mathbf{E} &= W_1^{1,1} \\ V_1 \mathbf{E} &= W_1^{0,2} + W_1^{1,1} \\ V_2 \mathbf{E} &= 2 W_2^{0,2} \end{aligned} \tag{3.3}$$

where $\mathbf{E} \equiv \hat{e}_1 \otimes \hat{e}_1 + \hat{e}_2 \otimes \hat{e}_2$ is the unit matrix used to raise the rank of the usual scalar MFs.

Eqn. 3.3 implies that for a single curve, $W_1^{1,1}$ is proportional to the identity matrix and does not provide any extra information over the area fraction. This will also hold for a set of non-overlapping curves. In a similar way, $W_2^{0,2}$ is also proportional to the identity matrix and does not provide any extra information over the genus. However, $W_2^{1,1}$ provides very useful shape information in addition to the information provided by the contour length. We explain in sections 3.5 and 3.6 how this information can be extracted from $W_2^{1,1}$.

## 3.4 Connected regions and holes in random fields

In this section, we explain how we can obtain a set of connected regions and holes from a given random field and apply MT statistics to the boundaries of these regions.

Consider a random field defined in flat 2D space. We can choose a threshold value, $\nu$, of the field and cut-off the field at this value. The regions which have field values greater than the threshold, form connected regions. The set of such regions for a given value of the threshold, together form an excursion set. The regions which have field values smaller than the threshold, but which are surrounded on all sides by regions with field values greater than the threshold, similar to a lake surrounded by land, are called holes. An example of excursion sets obtained from a random field in two dimensions is given in Fig. 3.2. The green curves represent the excursion set obtained by choosing a threshold value of 0, while the blue and red curves represent excursion sets for threshold values 0.6 and -0.6 respectively.

The boundaries of such regions form closed curves to which MT statistics can be applied. By studying the MTs of these excursion sets, one can test the statistical properties of the underlying random field. For example, if the field is Gaussian, then it will show up in the amplitude of the scalar MFs and the MTs. If the field is statistically isotropic, then it will show up in the intrinsic isotropy of the boundaries of excursion sets and their net relative alignment. However, this information will only be captured in the MTs and not in the scalar MFs. The next section explains how the MTs capture shape information from the closed curves.

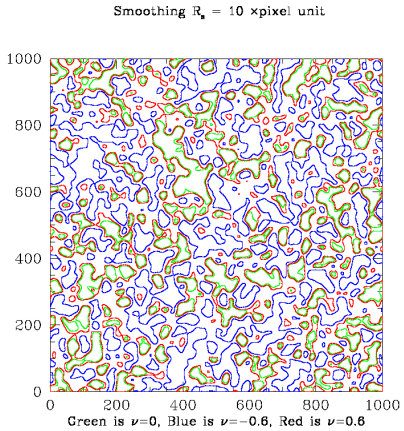


Figure 3.2: Sample excursion sets from a random field in 2D space.

## 3.5 Shape parameter $\beta$

Here we focus on the MT $W_2^{1,1}$ as it contains information regarding the shape of the closed curve [77]. The definition of $W_2^{1,1}$ for a single closed curve is given in Eqn. 3.2. Once we have computed the elements of $W_2^{1,1}$, we obtain the eigenvalues for this matrix. Let $\lambda_1$ and $\lambda_2$ denote the two eigenvalues such that $\lambda_1 \leq \lambda_2$. The eigenvalues do not change with the rotation of the curve. The shape parameter $\beta$ is then given by,

$$\beta \equiv \frac{\lambda_1}{\lambda_2} \tag{3.4}$$

It is important to note that the value of $\beta$ does not change upon scaling the size of the curve. $\beta$ gives a measure of the intrinsic isotropy of the curve. We can show that the value of $\beta$ is one for any closed curve with $m$-fold symmetry, for $m \geq 3$. Some examples of isotropic convex structures are circles, equilateral triangles and equi-angular $n$-polygons. By construction, the value of $\beta$ can not be greater than one. A value of $\beta$ smaller than one indicates deviation from isotropy. As an example, for an ellipse, the more elongated the ellipse, the smaller the value of $\beta$. In this way, $\beta$ quantifies the isotropy of a closed curve.

## 3.6 Alignment parameter $\alpha$

Here we discuss the relative alignment of a set of closed curves. First, we find $W_2^{1,1}$ for each individual curve. Then we average each individual element over all the closed curves to obtain the mean, $\overline{W}_2^{1,1}$. We denote the two eigenvalues of $\overline{W}_2^{1,1}$ as $\Lambda_1$ and $\Lambda_2$ such that

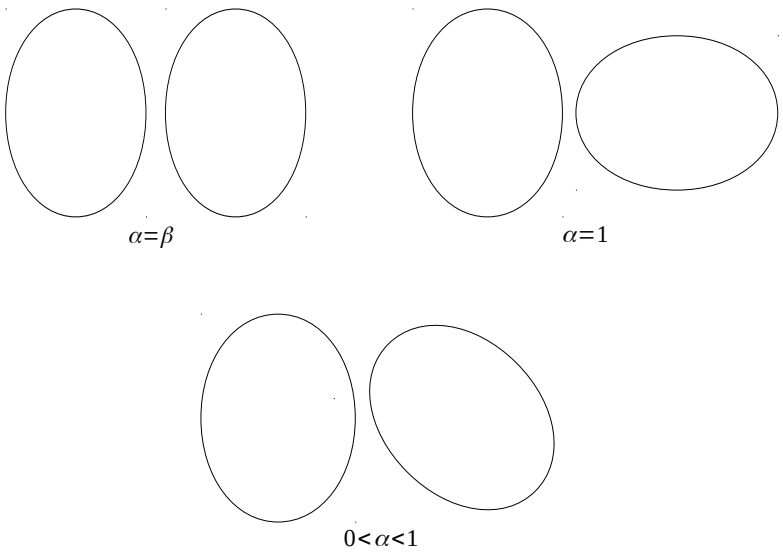


Figure 3.3: $\alpha$ for a set of two identical ellipses for different angles between their semi-major axes.

$\Lambda_1 \leq \Lambda_2$. The alignment parameter $\alpha$ is then defined as,

$$\alpha \equiv \frac{\Lambda_1}{\Lambda_2} \tag{3.5}$$

For a single curve, we find that $\alpha = \beta$. For any set of circles with arbitrary radii, it is straightforward to show that $\alpha = 1$.

$\alpha$ gives a measure of the relative alignment between individual curves that are intrinsically anisotropic. In order to explain this, we consider a set of two identical ellipses. Each individual ellipse has the same value of $\beta$, where $0 < \beta < 1$. In the first case, let the ellipses be arranged in such a way that their semi-major axes are orthogonal to each other. For this case, we find that $\alpha = 1$. Next, let the ellipses be arranged such that their semi-major axes are aligned in the same direction. In this case, $\alpha = \beta$. Finally, if the ellipses are arranged such that the angle between their semi-major axes is less than $90^\circ$, then we find that $0 < \alpha < 1$. These cases are demonstrated in Fig. 3.3.

To understand how $\alpha$ measures the statistical isotropy of the set of curves, we visualize the ellipses as follows. The translation invariance of $W_2^{1,1}$ allows us to translate one of the ellipses so that the two have a common centroid. We first find out the average radial distances of the ellipses from the centroid, in each direction. We then denote the curve formed by connecting the points which are at these average radial distances from the centroid in each direction, as the *locus curve*. We expect that for the set of ellipses, $\alpha = 1$, if their

locus curve is isotropic. However, if the two ellipses are not identical, then their locus will be anisotropic even if their semi-major axes are orthogonal to each other. In this case, we would not recover $\alpha = 1$ . We can extend this example to a distribution of ellipses and we would find that $\alpha = 1$ if the distribution is isotropic and $\alpha$ deviates from one when it is anisotropic. We can generalize this understanding to any spatial distribution of closed curves in flat 2D space and state that the distribution is statistically isotropic or unaligned if $\alpha = 1$ and anisotropic if $\alpha < 1$.

## 3.7 Summary

In this chapter, we have reviewed the definitions of the scalar MFs and the MTs for closed curves in flat 2D space. MTs are tensor generalizations of the usual scalar MFs. They contain additional information over their scalar coutnerparts. Of the three linearly independent and translation invariant MTs in flat 2D space, we have focused on $W_2^{1,1}$. For a single closed curve, $W_2^{1,1}$ contains information on its intrinsic isotropy. Intrinsic isotropy here refers to the $m$-fold rotational symmetry of the closed curve with $m \geq 3$. For a set of closed curves, $W_2^{1,1}$ contains inforamtion regarding the statistical isotropy or relative spatial alignment of the curves.

We provide a new way to visualize a spatial distribution of closed curves in the context of measuring statistical isotropy. The isotropy of the locus curve which we have defined, gives a measure of the statistical isotropy of the distribution of closed curves. We have explained this with examples of identical ellipses with different angles between their semi-major axes. We have also shown how the information regarding the intrinsic isotropy of individual curves and relative spatial alignment of a set of closed curves is encoded in the rank-2 MT $W_2^{1,1}$.

For a random field defined in flat 2D space, we have shown how excursion sets can be obtained by choice of suitable threshold field values. The boundaries of structures in the excursion sets form closed curves to which we can apply MT statistics. By studying the MTs of a random field and their dependence on threshold values, we can get useful insights into the properties of the field. This method can be applied to observational data of cosmological fields and can be used as a test of the standard $\Lambda$CDM cosmological model.

# 4

# MINKOWSKI TENSORS FOR RANDOM FIELDS ON THE SPHERE

## 4.1 Introduction

In chapter 3, we reviewed the definitions of the scalar MFs and the MTs for random fields in flat 2D space. We are interested in the application of MTs to cosmological data such as the CMB temperature fluctuations and Polarization and large scale structure. The CMB fields are defined on the sphere and so the expressions for the MTs mentioned in chapter 3 can not be directly applied to CMB data. In this chapter we shall discuss two ways of approaching this problem.

In the first method, as in [30], the CMB fields on the sphere are projected onto a two dimensional plane using a stereographic projection. Next, the boundaries of the excursion sets in the pixelized map are identified and the two dimensional MT statistics are applied to the projections of the fields onto the plane. This method is applied to the data and then to simulations based on the standard $\Lambda$CDM cosmological model. A comparison of the $\beta$ and $\alpha$ values obtained from data and from the simulations gives a measure of the agreement between the model and the data. In [30], the authors used this method and found good agreement between the data and the simulations for the CMB temperature fluctuations data from the *Planck* 2015 release. They found a 4-$\sigma$ difference between the simulations and *Planck* 2015 data for the *E* mode of CMB polarization.

It is important to know whether the stereographic projection has a significant contribution to the difference between data and simulations found in [30], before we investigate the

physical origin of such disagreement. In this context, we are interested in measuring the MTs for the CMB fields directly on the sphere. We do so by generalizing the definition of the MTs defined on flat space to closed curves on the surface of a sphere. The MTs are re-expressed in terms of the field derivatives which can be computed for every point in the field. This enables us to compute the average value of the MTs per unit area. We compute MTs for the data and for 100 $\Lambda$CDM simulations and compare the two to test the level of agreement.

This chapter is organized as follows, first we discuss the computation of the MTs using stereographic projection on to a plane, in section 4.2. In section 4.3, we generalize the definitions of MTs to general curved space and in particular, on the surface of a sphere. Then we calculate analytically the ensemble average of the MTs for isotropic Gaussian and Rayleigh fields on the sphere. We demonstrate how the MTs can be estimated numerically from a pixelated map, in section 4.5. Finally, in section 4.7, we apply this method to calculate the MTs directly on the sphere, to the *Planck* 2015 temperature fluctuations data and $\Lambda$CDM simulations and present a comparison of the two.

## 4.2 $\alpha$ for CMB data using stereographic projection

In this approach, the fields defined on the sphere are first projected on to a 2D plane. Then the MTs are calculated numerically from the projected fields. The mean of the shape parameter $\beta$, and the aligment parameter $\alpha$ can then be estimated from the eigenvalues of the MTs. Vidhya and Pravabati applied this method [30] to the CMB temperature fluctuations and *E* mode data given in the *Planck* 2015 data release. They found very good agreement, $\approx$ 1-$\sigma$ between the data and simulations based on the standard $\Lambda$CDM cosmological model for the temperature fluctuations data. For the *E* mode data, they found disagreement at the level of 4-$\sigma$ with the simulations. An understanding of the origin of this difference can lead to important cosmological insights.

The stereographic projection preserves the relative angles between the line elements of the closed curve, however the size of the structure can get scaled. For example, circles on the surface of a sphere are projected as circles on the plane with the size being scaled depending on the location on the sphere. This is demonstrated in Fig. 4.1. This means that the sizes of the hot and the cold spots can get scaled and it can lead to numerical artefacts in the calculations of $\alpha$ for these structures. Another issue is that with an increase in the level of anisotropy, the numerical errors associated with the pixelization of the field also

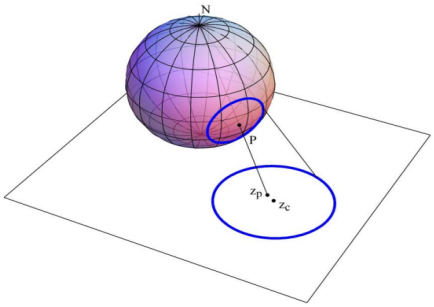


Figure 4.1: Stereographic projection of a circle on the sphere, on to a plane.

increase. This is seen in table 2 of [30]. For a pair of identical ellipses, the percentage numerical error in the computation of $\alpha$ increases as the major axes of the ellipses are more aligned. Higher alignment between the structures corresponds to a higher level of anisotropy. When the major axes of the ellipses are orthogonal to each other, which means the most isotropic case, the numerical error in compuation of $\alpha$ is $0\%$. In the case where the the major axes of the ellipses are aligned in the same direction, which means most anisotropic, the error in computation of $\alpha$ goes up to $24\%$.

By computing the MTs for the fields directly on the sphere, we can mitigate the numerical errors introduced by the stereographic projection of the field, leading to a more accurate estimate of the MTs. Before making physical inferences from the results of [30] for the CMB *E* mode data, it is important to check whether the disagreement persists even with direct a direct estimation of MTs on the sphere. It is also desirable to have an analytical understanding of the MTs for fields defined on curved spaces. For these reasons, we have developed a method for computing the MTs on the sphere and it is discussed in section 4.3.

## 4.3 Generalizing Minkowski Tensors to closed curves on the sphere

We begin by revisiting the definitions of the MTs in flat space. The linearly independent translation invariant MTs are given by [77],

$$W_1^{1,1} = \tfrac{1}{2}\int_C \vec{r}\otimes\hat{n}ds$$
$$W_2^{1,1} = \tfrac{1}{2}\int_C \vec{r}\otimes\hat{n}ds$$
$$W_2^{0,2} = \tfrac{1}{2}\int_C \hat{n}\otimes\hat{n}ds$$

From Eqn. 3.3, $W_1^{1,1}$ is proportional to the Identity matrix and does not provide any extra information over the scalar MFs. $W_2^{0,2}$ is also proportional to the Identity matrix, but its two diagonal elements provide independent tests of the Gaussianity of the field. $W_2^{1,1}$ contains very useful information about the shape of the structures. In this section, we will focus on the two MTs $W_2^{1,1}$ and $W_2^{0,2}$.

The expressions for $W_2^{1,1}$ and $W_2^{0,2}$ contain the position vector term, which is not well defined for a general curved manifold. The CMB fields are defined on the sphere and so these definitions of MTs can not be directly applied to them. In order to apply the MT statistics to the CMB fields, we must first generalize the definitions to the sphere. For any given curved manifold, the tangent vector space is defined at every point on the manifold. From this tangent vector space, a unique tangent vector is associated with each point on a curve. With this knowledge, we re-express the MTs in terms of the tangent vector and the curvature of the curve at each point by using integration by parts.

[79, 80] contain an introduction and study of integral geometry for tensors on spaces with affine connections. Tensor integration consists of parallel transporting the tangent vectors to a point on the curve and then adding them together in the same tangent vector space. It is defined as the inverse operation of covariant differentiation. With this notion of tensor integration, we define two quantities for a smooth closed curve on a general curved manifold as,

$$\mathcal{W}_1 \equiv \frac{1}{4}\int_C \hat{T}\otimes\hat{T}\,\mathrm{d}s$$

$$\mathcal{W}_2 \equiv \frac{1}{2\pi}\int_C \hat{T}\otimes\hat{T}\,\kappa\,\mathrm{d}s \tag{4.1}$$

$\hat{T}$ is the unit tangent vector at each point on the curve and $\kappa$ is the geodesic curvature of the curve at every point on the curve. $\mathcal{W}_1$ is the tensor generalization of the scalar MF contour length and we shall refer to it as the Contour Minkowski Tensor (CMT). $\mathcal{W}_2$ is the generalization of $W_2^{1,1}$ to any curved manifold in two dimensions. It is to be noted that while $W_2^{1,1}$ and $W_2^{0,2}$ contain the position vector, $\mathcal{W}_1$ and $\mathcal{W}_2$ depend only on the tangent vector and the geodesic curvature and can hence be applied to closed curves on the surface of a sphere. The work presented here has been published in [81].

## 4.4 Analytical computation of MTs on the sphere

In this section we will derive analytic expressions for the computation of the element by element average of $\mathcal{W}_1$ and $\mathcal{W}_2$ over all the closed curves for a given field on the sphere. We shall denote them by $\overline{\mathcal{W}}_1$ and $\overline{\mathcal{W}}_2$ respectively. We start with the generalized definitions given in Eqn. 4.1. With the introduction of a suitable Jacobian and the Dirac $\delta$-function , we convert the line integrals to area integrals, as done in [57], to get,

$$\overline{\mathcal{W}}_1 = \frac{1}{4}\int_{S^2} \mathrm{d}a\, \delta(u-\nu_t)\, |\nabla u|\, \hat{T}\otimes\hat{T} \tag{4.2}$$

$$\overline{\mathcal{W}}_2 = \frac{1}{2\pi}\int_{S^2} \mathrm{d}a \delta(u-\nu_t)\kappa\, |\nabla u|\, \hat{T}\otimes\hat{T} \tag{4.3}$$

where $u$ is the field, $\nu_t$ is the threshold, and $\mathrm{d}a$ is the area element. If we can express the tangent vector in terms of the field, then the whole of the integrand would be in terms of the field and we can perform the analytic calculation. This can be achieved as follows. For each point on the curve, the normal vector can be given as $\vec{n} = \nabla u = (u_{;1}, u_{;2})$, where $n$ is the normal vector, $\nabla$ denotes the covariant derivative on the sphere and $u_{;i}$ is the $i$-th component of the covariant derivative. The tangent vector is orthogonal to the normal vector and hence we can choose to write it in terms of the field as,

$$\hat{T}_i = \epsilon_{ij}\,\frac{u_{;j}}{|\nabla u|} \tag{4.4}$$

$\epsilon_{ij}$ denotes the antisymmetric tensor and $\epsilon_{12} = 1$. As explained in [81], $\kappa$ can be written in terms of the field derivatives as,

$$\kappa = \frac{2u_{;1}u_{;2}u_{;12} - u_{;1}^2 u_{;22} - u_{;2}^2 u_{;11}}{|\nabla u|^3} \tag{4.5}$$

By substituting Eqns. 4.4 and 4.5 in Eqns. 4.2 and 4.3, we obtain

$$\overline{\mathcal{W}}_1 = \frac{1}{4}\int_{S^2} \mathrm{d}a\, \delta(u-\nu_t)\frac{1}{|\nabla u|}\mathcal{M} \tag{4.6}$$

$$\overline{\mathcal{W}}_2 = \frac{1}{2\pi}\int_{S^2} \mathrm{d}a\, \delta(u-\nu_t)\frac{\kappa}{|\nabla u|}\mathcal{M} \tag{4.7}$$

the matrix $\mathcal{M}$ denotes the tensor product $\hat{T}\otimes\hat{T}$ and can be given as

$$\mathcal{M} = \begin{pmatrix} u_{;2}^2 & u_{;1}u_{;2} \\ u_{;1}u_{;2} & u_{;1}^2 \end{pmatrix} \tag{4.8}$$

Even though the determinant of $\mathcal{M}$ vanishes at each point on the sphere, we can show that the determinants of $\overline{\mathcal{W}}_1$ and $\overline{\mathcal{W}}_2$ will not be zero. The off-diagonal elements $u_{;1}u_{;2}$ will be zero when $u_{;1}$ and $u_{;2}$ are not correlated. For such a case, the diagonal elements of $\overline{\mathcal{W}}_1$ and $\overline{\mathcal{W}}_2$ will be their eigenvalues and their product will give the respectively determinants.

For a random field on the surface of a sphere, Eqns. 4.6 and 4.7 can be used to analytically compute the MTs. In section 4.5, we discuss the numerical estimation of these quantities from pixelated maps.

### 4.4.1 Ensemble expectation values for isotropic Gaussian fields

Here we shall compute the ensemble expectation values per unit area of the MTs for an isotropic Gaussian field $u$, defined on the surface of a sphere. For this we need the joint Probability Distribution Function (PDF) of the field and it's derivatives. Let $\xi(r)$ denote the two point function of $u$ with $r$ ebing the distance between the two points. The variance of the field and it's derivatives can be expressed in terms of $\xi(r)$ as,

$$\sigma_0^2 = \left\langle u^2 \right\rangle = \xi(0)$$

$$\sigma_1^2 = \left\langle |\nabla u|^2 \right\rangle = 2\xi''(0)$$

$$\sigma_2^2 = \left\langle \left|\nabla^2 u\right|^2 \right\rangle = 2\xi''''(0) \tag{4.9}$$

$'$ represents differentiation with respect to $r$. Let $\vec{X}$ denote the vector consisting of $u$ and its first and second order derivatives. We have $\vec{X} = (u, u_{;1}, u_{;2}, u_{;11}, u_{;22}, u_{;12})$ with a joint probability distribution given as,

$$\mathrm{P}(\vec{X}) = \frac{1}{\sqrt{(2\pi)^6 \det\Sigma}} \exp -\frac{1}{2}\left(\vec{X}\Sigma^{-1}\vec{X}\right) \tag{4.10}$$

and the covariance matrix $\Sigma$ is given [53] as,

$$\Sigma = \begin{pmatrix} \sigma_0 & 0 & 0 & -\sigma_1/2 & -\sigma_1/2 & 0 \\ 0 & \sigma_1/2 & 0 & 0 & 0 & 0 \\ 0 & 0 & \sigma_1/2 & 0 & 0 & 0 \\ -\sigma_1/2 & 0 & 0 & \sigma_2/2 & \sigma_2/6 & 0 \\ -\sigma_1/2 & 0 & 0 & \sigma_2/6 & \sigma_2/2 & 0 \\ 0 & 0 & 0 & 0 & 0 & \sigma_2/6 \end{pmatrix} \tag{4.11}$$

We can then write the ensemble expectation values of the MTs for each threshold $\nu_t$ as,

$$\begin{aligned} \left\langle \overline{\mathcal{W}}_1(\nu_t) \right\rangle &= \int \mathrm{d}\vec{X}\, \mathrm{P}(\vec{X}) \int_{S^2} \mathrm{d}a\, \delta(u-\nu_t)\, \tfrac{1}{|\nabla u|}\, \mathcal{M} \\ \left\langle \overline{\mathcal{W}}_2(\nu_t) \right\rangle &= \int \mathrm{d}\vec{X}\, \mathrm{P}(\vec{X}) \int_{S^2} \mathrm{d}a\, \delta(u-\nu_t)\, \tfrac{\kappa}{|\nabla u|}\, \mathcal{M} \end{aligned} \tag{4.12}$$

The field $u$ is isotropic and hence the area integral and the $\vec{X}$ integrals commute, allowing us to perform the $\vec{X}$ integral first. This gives us the ensemble expectation values of $\overline{\mathcal{W}}_1$ and $\overline{\mathcal{W}}_2$ per unit area,

$$\begin{aligned} \left\langle \overline{w}_1(\nu_t) \right\rangle &= \tfrac{1}{16\sqrt{2}r_c}\, e^{-\nu_t^2/2}\, \mathcal{I} \\ \left\langle \overline{w}_2(\nu_t) \right\rangle &= \tfrac{1}{8\sqrt{2}\pi^{3/2}r_c^2}\, \nu\, e^{-\nu_t^2/2}\, \mathcal{I} \end{aligned} \tag{4.13}$$

where $r_c \equiv \sigma_0/\sigma_1$ is the correlation length and $\mathcal{I}$ is the identity matrix. The alignment parameter at every threshold is $\alpha = \left\langle \overline{w}_1 \right\rangle_{11} / \left\langle \overline{w}_1 \right\rangle_{22} = 1$.

For any Gaussian field isotropic or not, $u_{;1}$ and $u_{;2}$ are always uncorrelated and hence the diagonal terms of $\langle \overline{w}_1(\nu_t) \rangle$ are always zero. The diagonal elements of $\langle \overline{w}_1(\nu_t) \rangle$ contain information on the Gaussian nature of the field. The correlation length $r_c$ contains cosmological information. The statistical isotropy (SI) of the field is captured by the equality of the diagonal elements of $\langle \overline{w}_1(\nu_t) \rangle$. For an isotropic field, $\alpha = 1$, and $0 < \alpha < 1$ for an anisotropic field. The diagonal elements of $\langle \overline{w}_2(\nu_t) \rangle$ are always identical irrespective of the level of isotropy of the field. Eqn. 4.13 is valid for flat and curved spaces alike.

### 4.4.2 Ensemble expectation values for isotropic Rayleigh fields

For the CMB, the total polarization intensity has a Rayleigh PDF. Thus it is important to have an analytical understanding of the MTs for Rayleigh fields on the sphere before we apply MT statistics to the CMB polarization field. The approach we take is similar to the one in section 4.4.1. Let $Q$ and $U$ denote the usual stokes parameters for the CMB

polarization field, then we construct the 12 dimensional vector $\vec{Y}$ from $Q$, $U$ and their derivatives, $\vec{Y} = (Q, U, Q_{;i}, U_{;i}, Q_{;ij}, U_{;ij})$, where $i, j = 1, 2$. The joint PDF of $\vec{Y}$ can then be given as,

$$\mathrm{P}(\vec{Y}) = \frac{1}{\sqrt{(2\pi)^{12}\mathrm{det}\Sigma}} \exp\left(-\frac{1}{2}\vec{Y}\,\Sigma^{-1}\,\vec{Y}\right) \tag{4.14}$$

where $\Sigma$ is the covariance matrix for a Rayleigh distribution (expression for $\Sigma$ is given in section 2.2 of [82]). We then calculate the integrals in a similar way as in 4.4.1 to get,

$$\begin{aligned} \langle \overline{w}_1(\nu_t) \rangle &= \tfrac{1}{2r_c} \nu\, e^{-\nu_t^2/2}\, \mathcal{I} \\ \langle \overline{w}_2(\nu_t) \rangle &= \tfrac{1}{8\pi r_c^2} \left(\nu_t^2 - 1\right) e^{-\nu_t^2/2}\, \mathcal{I} \end{aligned} \tag{4.15}$$

The information contained in $\langle \overline{w}_1(\nu_t) \rangle$ and $\langle \overline{w}_2(\nu_t) \rangle$ here is to be interpreted in the same way as in section 4.4.1.

## 4.5 Numerical estimation of $\alpha$

When dealing with real data, the maps are pixelated and Eqns. 4.6 and 4.7 can not be directly applied. We compute the MTs numerically for these maps. Before we can compute MTs numerically for pixelated maps, we need to find a suitable approximation for the $\delta$-function. We follow the method in [57] and approximate the $\delta$-function as follows:

$$\delta(u - \nu_t) = \frac{1}{\Delta\nu_t} \tag{4.16}$$

for pixels having the value of the field between $\nu_t - \Delta\nu_t/2$ and $\nu_t + \Delta\nu_t/2$. $\Delta\nu_t$ is the size of the bin for the threshold. For the rest of the pixels, $\delta\nu_t = 0$.

The approximation of the $\delta$-function introduces a numerical error in the estimation of the MTs. This error has been studied and quantified in [83]. Let $\overline{\mathcal{W}}_1^{Gauss}$ denote the matrix obtained for a Gaussian isotropic field using Eqn. 4.13 . Then the numerical error in the diagonal elements of $\overline{\mathcal{W}}_1$ associated with the approximation of the $\delta$-function, $\Delta\overline{\mathcal{W}}_1$, can be given by [83],

$$\Delta\overline{\mathcal{W}}_1 = \frac{\sqrt{\pi}}{4\sqrt{2}} \frac{\sqrt{\tau}}{\Delta\nu} \left(\mathrm{erf}(\nu_+) - \mathrm{erf}(\nu_-)\right) - \overline{\mathcal{W}}_1^{Gauss} \tag{4.17}$$

where $\nu_+ = \nu + \Delta\nu/2$ and $\nu_- = \nu - \Delta\nu/2$.

We simulated an isotropic Gaussian CMB temperature map and computed $\overline{\mathcal{W}}_1$ analytically based on Eqn. 4.13 and numerically based on Eqn. 4.6. By taking the difference

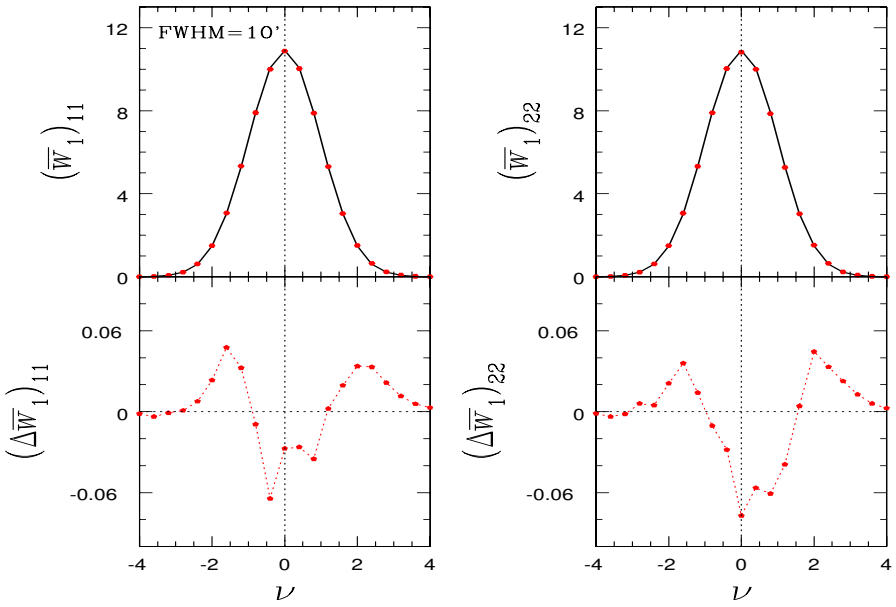


Figure 4.2: *Top panel*: Diagonal elements of $\overline{\mathcal{W}}_1$ from one simulated isotropic Gaussian CMB temperature fluctuations map. The black solid line represents the analytic calculation using Eqn. 4.13, while the red dots represent the numerical computations using Eqn. 4.6. *Bottom panel*: Numerical error in the respective elements obtained by subtracting the numerical results from the corresponding analytic ones. The error is in good agreement with what is expected from the $\delta$-function approximation.

of $\overline{\mathcal{W}}_1$ computed by these two methods, we found that the error is in good agreement with what is expected from the $\delta$-function approximation as given in [83]. This is shown in Fig. 4.2. By using this approximation for the $\delta$-function in Eqn. 4.6, we can compute $\alpha$ numerically for a pixelated map.

## 4.6 Application to CMB simulations

We want to use Eqn. 4.6 to numerically estimate $\alpha$ for the CMB temperature fluctuations data given in the *Planck* 2015 data release [13]. But first we apply our method to simulated Gaussian CMB maps with input isotropic power spectrum in order to test the reliability of our method. For these maps it is expected that we should recover $\alpha$ values close to one. In this section, we will study the effect of the Galactic and point sources mask, beam smoothing and the pixel size on the estimation of $\alpha$ as a function of the threshold.

### 4.6.1 Galactic and point sources mask

The level of foreground contamination is very high for regions close to the Galactic plane. For such regions, recovering the clean CMB signal is difficult and hence they are excluded from cosmological analysis along with the pixels that contain point sources. In our analysis, we use the common mask UT78, which is given by the *Planck* team [13] as the preffered mask for temperature analysis. UT78 has a sky fraction of 77.6%. When excluding some regions of the sky from the analysis, closed curves near the boundaries of these regions can get cut off and contribute junk values to the estimation of $\alpha$. Understanding the impact of masking on the estimation of $\alpha$ is important. We study this effect with the help of simulations.

First we generate 100 realizations of the CMB temperature sky with FWHM=$20'$ using the HEALPIX [36, 37] package along with the CMB angular power spectrum from the CAMB [47, 48] package. We compute $\alpha$ for each realization and the mean $\overline{\alpha}$ and standard deviation $\sigma_\alpha$ over the 100 realizations. $\overline{\alpha}$ obtained in this way is represented by the blue line in the top left panel of Fig. 4.3 . $\alpha$ values for thresholds further away from the mean are found to be relatively smaller than those for thresholds closer to the mean. This is because there are fewer structures away from the mean that $\alpha$ is avergaed over and the probability of them being isotropically distributed is very small. We then mask the simulations with the UT78 and and compute $\overline{\alpha}$ and $\sigma_\alpha$ for the masked maps. These are represented in the top left panel of Fig. 4.3 by the red line. $\overline{\alpha}$ values for the masked simulations are found to be relatively smaller than those for the unmasked ones. This result is expected since masking removes regions of the sky from the analysis. This leads to $\alpha$ being averaged over fewer structures and hence a larger statistical error.

### 4.6.2 Beam smoothing

The observing instrument can contribute residual noise to the CMB data leading to an inaccurate estimation of $\alpha$. In order to mitigate this effect, the maps are smoothed with a Gaussian beam with a suitable FWHM. Smoothing also provides a way to reduce the effect to closed curves that get cut off at the mask boundaries, on the estimation of $\alpha$. Here we discuss how smoothing affects the estimation of $\alpha$. We repeat the procedure mentioned in section 4.6.1 and calculate $\alpha$ for the masked simulations with a different smoothing angle of $60'$. These are represented in the top right panel of Fig. 4.3 by the red line, while the blue line represents masked simulations with an FWHM of $20'$. The maps smoothed with FWHM=$60'$ are found to have $\alpha$ values relatively smaller than those with FWHM=$20'$.

Smoothing reduces the number of structures that $\alpha$ is averaged over, leading to a larger statistical error in the estimation of $\alpha$.

### 4.6.3 Pixel size

When smoothing a map, it is decomposed into spherical harmonics and these are convolved with a Gaussian beam of the given FWHM. During this process, it is important to make sure that the smoothing scale is not very large in comparison with the size of a pixel. We compare $\alpha$ obtained from the SMICA CMB temperature data and $\overline{\alpha}$ averaged over 100 pure CMB simulations, each with the HEALPIX resolution parameter $N_{side}$=2048, with and without first downgrading the maps to $N_{side}$=512. We find a better agreement between the data and the simulations when the maps are downgraded to $N_{side}$=512. The reason for this is not well understood.

In order to demonstrate this effect, we compare $\overline{\alpha}$ computed from 100 pure CMB simulations with $N_{side}$=1024, with that obtained from the same set of simulations after first downgrading them to $N_{side}$=512. The maps were smoothed with a Gaussian beam of FWHM=$20'$ in both the cases. They are represented by the blue and red lines respectively in the bottom middle panel of Fig. 4.3. We found that $\overline{\alpha}$ values for maps that were downgraded were lower than for those that were not. This is expected because the process of downgrading is similar to that of beam smoothing and leads to fewer structures that $\alpha$ is averaged over.

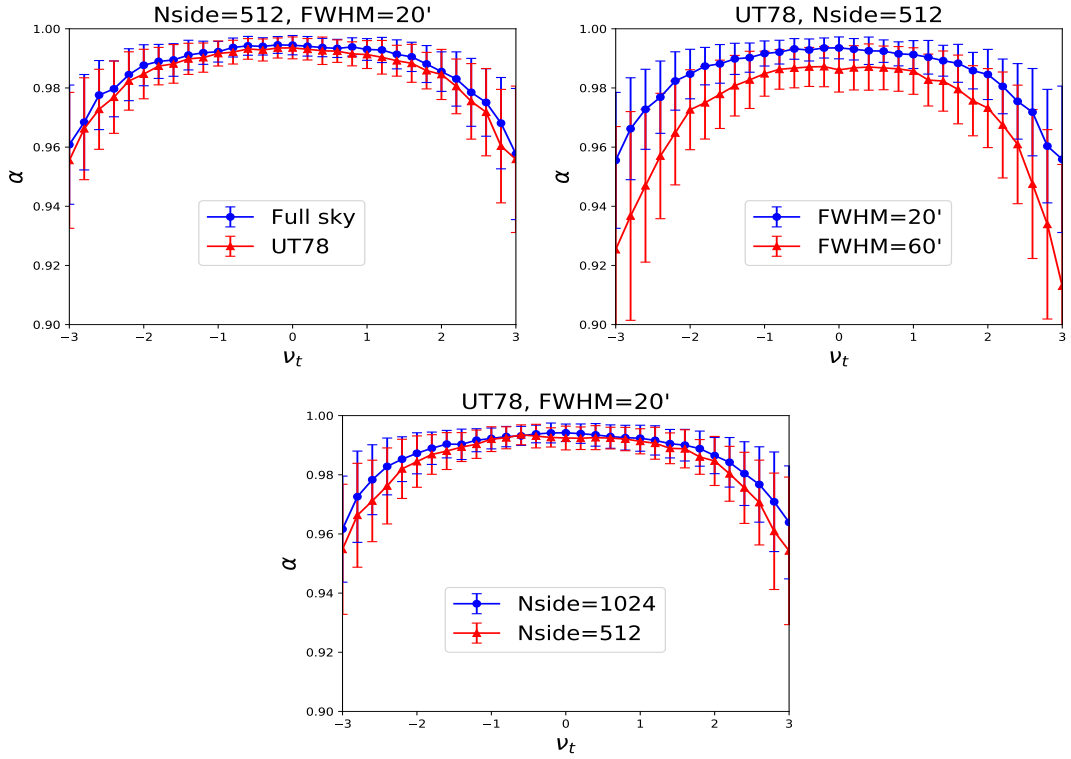


Figure 4.3: *Top left panel*: Comparison of $\overline{\alpha}$ for simulated CMB temperature maps smoothed to FWHM=$20'$, for unmasked (blue line) and masked (red line) simulations. *Top right panel*: Comparison of $\overline{\alpha}$ for masked CMB temperature simulations smoothed to FWHM=$20'$ (blue line) and FWHM=$60'$ (red line). *Bottom panel*: Comparison of $\overline{\alpha}$ values computed from CMB temperature simulations having $N_{side}$=1024 and FWHM=$20'$, with and without downgrading to $N_{side}$=512. All plots are results of averaging over 100 realizations. The error bars are the sample variance for 100 realizations.

## 4.7 Application to *Planck* data

In this section, we apply our method to the CMB temperature fluctuations data given in the *Planck* 2015 data release. The results presented here are on arxiv [84] and has been accepted for publication at JCAP. We want to test the SI of the observed data by comparing $\alpha$ obtained from the observations to the $\overline{\alpha}$ obtained from mock *Planck* data. The observations and simulations are first masked with UT78, downgraded to Nside=512, smoothed with a Gaussian beam of FWHM=$20'$ and then $\alpha$ is computed from them. The numerical error in $\alpha$ due to the $\delta$-function approximation mentioned in section 4.5 is well understood [83] and is almost identical for all the realizations with the same resolution. Hence it does not affect the estimation of the difference in $\alpha$ values between the data and the simulations and we have not subtracted this error. In all the figures here, $\alpha$ is used to denote both the $\alpha$ from the data as well as the $\overline{\alpha}$ from the simulations.

### 4.7.1 SMICA CMB temperature map

We have used the CMB temperature map provided by the SMICA pipeline [39, 40]. It has a resolution of Nside=2048 and FWHM=$5'$. The map is downgraded to Nside=512, smoothed with a Gaussian beam of $20'$ and masked with the common mask UT78. Next, we estimate $\alpha^{data}$ from this map and it is represented by the red line in Fig. 4.4. For the mock data, we take 100 publicly available Full Focal Plane (FFP8) SMICA simulated maps including the instrument beam effect and residual foreground and noise. We then downgrade these maps to Nside=512, smooth them with a Gaussian beam of $20'$ and mask them with UT78 before computing $\alpha^{sim}$ from them. It is represented by the black line in Fig. 4.4. A comparison of the data and the FFP8 SMICA simulations both of which contain the CMB, instrument effects and residual foreground and noise, yields an excellent agreement, $\leq 1$-$\sigma$, between the data and the simulations. A comparison of $\alpha^{data}$ and $\alpha^{sim}$ computed from 100 pure CMB simulations leads to the same conclusion.

### 4.7.2 Individual frequency data

Here we test for alignment of structures in the beam-convolved CMB temperature maps at individual observing frequencies. *Planck* observes the CMB sky in nine frequency channels [38], ranging from 30 GHz to 857 GHz. We shall denote these by $T^{obs}$. There are four main algorithms which are used to extract the clean CMB signal from the total sky temperature [13]. They are Commander [41, 42], NILC [43, 44], SEVEM [45, 46] and SMICA [39, 40] and provide CMB subtracted maps for each observation frequency of *Planck*, which we

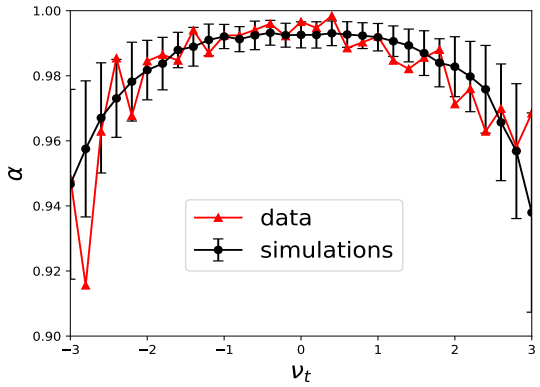


Figure 4.4: Comparison of $\alpha$ estimated from the SMICA CMB temperature map (red line), and $\alpha^{\text{sim}}$ computed from 100 FFP simulations (black line).

shall denote by $T^{fg}$. The clean beam-convolved CMB maps for each frequency, $T^{clean}$, are then obtained by subtracting the foreground maps from the observed sky temperature maps as,

$$T^{clean} \equiv T^{obs} - T^{fg} \tag{4.18}$$

The frequencies ranging from 30 GHz to 70 GHz are referred to as the Low Frequency Instrument (LFI) channels while those from 100 GHz to 857 GHz are referred to as the High Frequency Instrument (HFI) channels. The LFI data have a resolution of $N_{side} = 1024$ and the HFI data have a resolution of $N_{side} = 2048$. In our analysis, we first downgrade all the maps to a resolution of $N_{side} = 512$, mask them with UT78 and smooth them with a Gaussian beam of FWHM=$20'$ and then compute MTs from them. *Planck* also provides simulations of the CMB sky for all the LFI and HFI channels. We repeat the same procedure for the simulated data and compare the $\alpha$ computed from individual frequency data to those computed from the corresponding simulations. The results for individual frequency channels are plotted in figure 4.5.

To interpret the SI of the observational data described above, we compare them with mock *Planck* data. We compute $\alpha$ for 100 FFP9 simulations of the CMB temperature sky given in [38] for each individual observing frequency. A comparison of the data, which contains CMB and instrument beam effects, with the FFP9 simulations containing the same is shown in figure 4.5. The FFP9 simulations are represented by the black lines while the maps cleaned by the Commander, NILC, SEVEM and SMICA pipelines are represented by the purple, blue, green and red lines respectively. As mentioned earlier, $\alpha^{\text{sim}}$ is the mean over 100 simulations. $\sigma_\alpha$ is the standard deviation over the 100 simulations and is used as

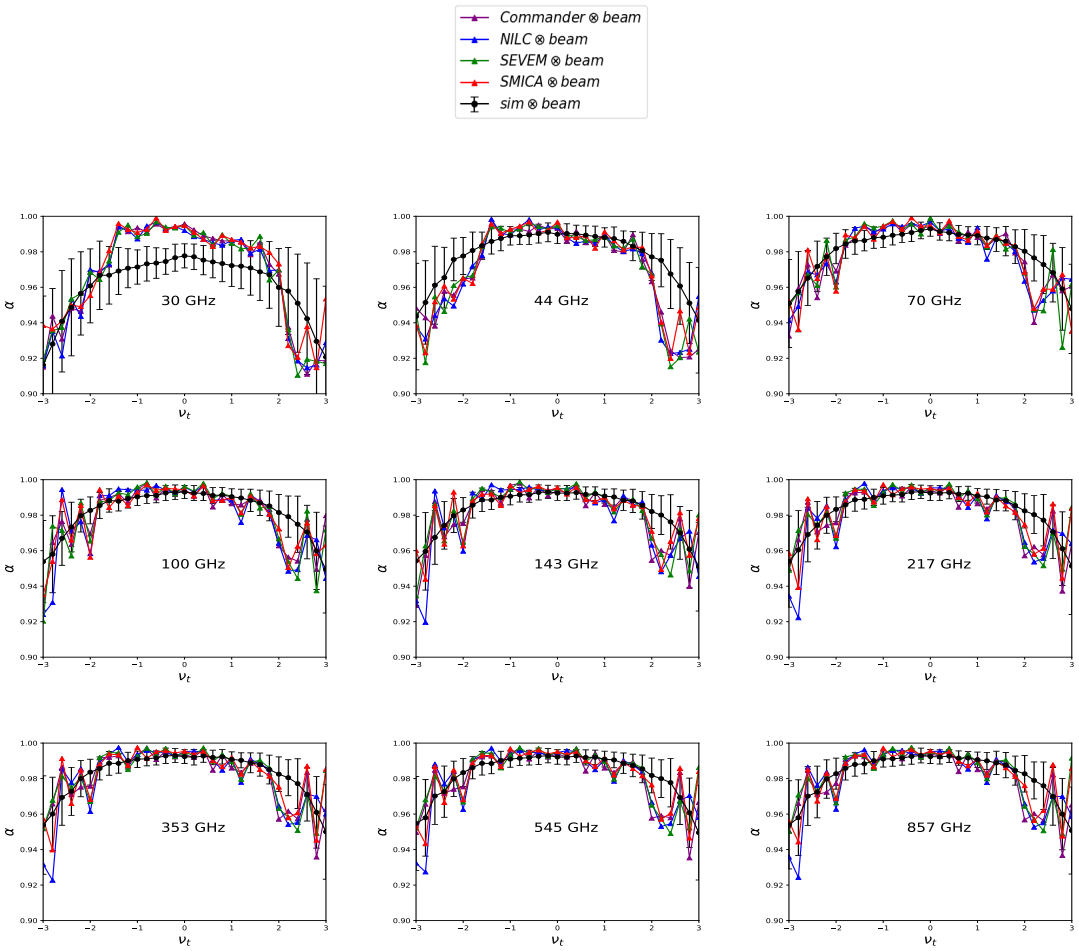


Figure 4.5: Comparison of $\alpha^{\mathrm{data}}$ for the *Planck* observation frequencies with $\alpha^{\mathrm{sim}}$ for beam-convolved CMB temperature maps from 100 *Planck* simulations for the corresponding frequencies. There seems to be good agreement between the data and the simulations which include the instrumental beam effect for all frequency channels, except 30 GHz.

the 1-$\sigma$ error bar in our analysis.

$\alpha$ values for thresholds further away from the mean are relatively smaller, as explained in section 4.6.1. We find that the $\alpha$ computed from the data is consistent with that computed from the corresponding simulations at the level of 1-$\sigma$, for the frequencies ranging from 44 GHz to 857 GHz. However, there is significant difference ($\approx$ 2-$\sigma$) between the $\alpha$ values computed from the data and the simulations for the case of the 30 GHz channel. The reason for this disagreement is not yet understood, but we suspect that an inaccurate estimation of the beam effect in the maps could be causing it. In order to confirm the source of this disagreement, we need a better understanding of the dependence of $\alpha$ on the instrument beam effect. We also find the same trends in the results when the procedure is repeated for each frequency channel with the maps being smoothed to an FWHM of $60'$. The estimation of $\alpha$ is not strongly affected by the addition of noise to the simulations for frequencies upto 353 GHz. Although, the addition of noise drastically affects the $\alpha$ estimates for the 545 GHz and 857 GHz simulations. This is expected because for the 545 GHz and 857 GHz channels, the CMB signal to noise ratio is smaller.

### 4.7.3 Quantifying the difference between data and simulations

The quantity $D_\alpha$ defined below gives a measure of the deviation of the data from the simulations,

$$D_\alpha \equiv \left| \frac{\alpha^{\,\mathrm{data}} - \alpha^{\,\mathrm{sim}}}{\sigma_\alpha^{\mathrm{sim}}} \right| \tag{4.19}$$

where the superscripts, "data" and "sim" denote the observed data and the *Planck* $\Lambda$CDM simulations respectively. Again, $\sigma_\alpha$ is the 1-$\sigma$ error bar, which is the standard deviation computed from the 100 simulations. $D_\alpha$ measures the level of disagreement between the data and the simulations. A smaller $D_\alpha$ value indicates good agreement between the theory and the observed data. $\overline{\mathcal{W}}_1$ is averaged over fewer structures for thresholds away from the mean as explained in section 4.6.1. Hence $\alpha$ values calculated for these thresholds are less significant. To get an accurate estimate of the level of agreement between the data and the simulations, the $D_\alpha$ values should be averaged over a range of thresholds for which the $\alpha$ values are highly significant. We average $D_\alpha$ over the threshold range: - 0.8 to + 0.8, for each dataset. For the maps smoothed with a Gaussian beam of FWHM=$20'$, the $D_\alpha$ values are listed in Table 4.1. If we choose to averaged $D_\alpha$ over the threshold range: - 1 to + 1, then the disagreement between the simulations and the observed data is reduced. However, there is still a significant disagreement $\approx$ 1.9-$\sigma$ for the 30 GHz channel.

| $\mathcal{D}_\alpha$ | 30 GHz | 44 GHz | 70 GHz | 100 GHz | 143 GHz | 217 GHz | 353 GHz | 545 GHz | 857 GHz |
|---|---|---|---|---|---|---|---|---|---|
| COM | 2.03 | 0.59 | 0.63 | 0.73 | 0.75 | 0.66 | 0.67 | 0.70 | 0.73 |
| NILC | 1.89 | 0.82 | 0.71 | 0.63 | 0.68 | 0.75 | 0.76 | 0.75 | 0.77 |
| SEVEM | 2.01 | 0.60 | 0.69 | 0.66 | 0.72 | 0.69 | 0.67 | 0.65 | 0.71 |
| SMICA | 2.01 | 0.69 | 0.78 | 0.70 | 0.61 | 0.60 | 0.62 | 0.61 | 0.61 |

Table 4.1: $\mathcal{D}_\alpha$ values averaged over thresholds, $\nu_t$, from $-0.8$ to $+0.8$, for CMB temperature for various *Planck* datasets smoothed with a Gaussian beam of FWHM=$20'$.

## 4.8 Summary

MTs contain additional shape information over their scalar counterparts. While the scalar MFs have been used in cosmology to study properties such as the Gaussian nature of cosmological fields, MTs provide a means to test the SI of these fields. The usual definitions of the 2D linearly independent translation invariant MTs contain a position vector term, which is not well defined for curved spaces. This means that the MT statistics can not be directly applied to the CMB fields which are defined on the sphere. In [30], the authors applied the MT method to the CMB temperature fluctuations and *E* mode fields by first projecting these fields on to a plane. They found good agreement between the data and the simulations for the temperature maps, but the *E* mode data was found to deviate from the $\Lambda$CDM simulations at the level of 4-$\sigma$. It is important to gain an analytical understanding and numerical estimation of MTs for random fields directly on the sphere before interpreting the SI of the data.

We have generalized the definitions of the MTs to curved spaces. This is achieved by using integration by parts in the usual definitions of the MTs and re-expressing them in terms of the tangent vector, which is always well defined for any curved space. By converting the line integrals in the MT definitions to area integrals with the use of a suitable Jacobian, we are able to re-write the definitions in a form which can be easily computed for

any smooth random field. It allows for the direct computation of the MTs for CMB fields which are defined on the surface of a sphere. We also describe a method for the numerical estimation of the MTs for pixelated maps on the sphere, by using an approximation for the $\delta$-function as in [57]. We have computed the ensemble average of the MTs $\mathcal{W}_1$ and $\mathcal{W}_2$ for isotropic Gaussian and Rayleigh fields on the sphere. The information on the SI of the field is contained in the equality of the eigenvalues of $\mathcal{W}_1$, while information on the Gaussian/Rayleigh nature is encoded in the amplitude of the expression for $\overline{\mathcal{W}}_1$. The diagonal elements of $\overline{\mathcal{W}}_2$ also provide independent probes of the Gaussianity of the field. This work has been published in the Journal of Cosmology and Astroparticle Physics (JCAP) [81].

We have applied the method described above to the CMB temperature fluctuations data given as part of the *Planck* 2015 data release [38]. We first used our method to compute the alignment parameter $\alpha$ from simulations and investigate the effect of masking, beam smoothing and pixel size on the estimation of $\alpha$. We define the quantity $D_\alpha$ which gives a measure of the level of disagreement between the observations and the simulations. Section 4.7.1 describes the application of this method to the CMB temperature fluctuations map provided by the SMICA pipeline and a comparison of the $\alpha$ thus obtained, to those obtained from the FFP8 simulations. The data is found to agree well with the simulations, $\leq$1-$\sigma$. Further, we compare the $\alpha$ values estimated from the beam-convolved maps at individual frequencies given in the *Planck* data, with the corresponding FFP9 simulations. We find good agreement $\approx$1-$\sigma$ between the data and the simulations for all frequencies except 30 GHz. The $\alpha$ values estimated from the 30 GHz data differ by $\approx$2-$\sigma$ from those estimated from the correspoding simulations. The origin of this difference is not well understood but we suspect that it could arise due to an inaccurate estimation of the beam effect. This work is on arxiv [84] and has been accepted for publication at JCAP.

# 5

# MINKOWSKI TENSORS AS TOOLS FOR CONSTRAINING REDSHIFT SPACE DISTORTION

## 5.1 Introduction

MTs statistics can be used to probe statistical properties such as Gaussianity and isotropy of random fields. They carry shape and direction information that is not there in the scalar MFs. The previous chapter describes the generalization of MTs to random fields on the sphere and application to the CMB temperature fluctuations field. These statistics were applied to non-Gaussian density fields constructed from slices of mock galaxy simulations in [85]. These fields contain a preferred direction because of the redshift space distortion effect, which is discussed below.

When the positions of a spatial distribution of galaxies is plotted in redshift space, the distribution appears squashed. This is because of the peculiar velocities of the galaxies causing a Doppler shift in addition to the cosmological redshift and is known as Redshift Space Distortion (RSD). The Hubble's law which relates observed redshifts to distances then gives an inaccurate estimate of the distance to the object. For galaxies that are bound in a virialized system, the Doppler shift associated with their peculiar velocities causes the system to appear elongated along the line of sight. This effect is called the "Fingers of God" effect. When a galaxy cluster assembles, the galaxies fall inwards towards the center of the cluster and the Doppler shift associated with their motion causes the system to look

squashed along the line of sight. This effect is known as the Kaiser effect.

In [85], the three dimensional density field was decomposed into two dimensional slices before applying MT statistics. This method is useful for photometric redshift catalogs which have large galaxy number density and volumes, but relatively poor information on the position along the line of sight. It is possible to directly analyze the full three dimensional density field due to the large spectroscopic galaxy catalogs becoming available [86–89]. The full three dimensional field contains more information than the slices that it is divided into. Additionally, the two and three dimensional statistics are expected to have a different sensitivity to bias, shot noise and redshift space distortion. Hence it is desirable to perform the analysis of the full field without binning it into two dimensional slices.

In this chapter, we apply the MT statistics to random fields in three dimensions. First, we derive an analytic expression for estimating MTs from a three dimensional density field and compute the ensemble expectation values of the MTs for isotropic Gaussian fields. We then give a numerical and a semi-analytic method to estimate MTs from a discretely sampled three dimensional field and apply our method to an isotropic Gaussian field in three dimensions. Finally, we study the effect of anisotropy of the field on the MTs and show that the MTs can constrain the linear redshift space distortion parameter. RSD modifies the shape of large scale structures along the line of sight of the observer and generates anisotropic iso-density contours. Here we use the three dimensional rank two translation invariant MTs $W_1^{0,2}$ and $W_2^{0,2}$ to search for the anisotropy generated by RSD. We calculate the ensemble average of $W_1^{0,2}$ and $W_2^{0,2}$ for an isotropic Gaussian field and also demonstrate a method to estimate these MTs from a discretely sampled field by generating iso-density surfaces. We discuss the effect of the linear RSD operator on $W_1^{0,2}$, $W_2^{0,2}$ and how it can be used to constrain the RSD parameter.

This chapter is organized as follows. In section 5.2, we review the definitions of the MTs in three dimensions. We compute the ensemble average of the MTs for an isotropic Gaussian random field in section 5.3. Section 5.4 contains a description of the algorithm that we use to numerically estimate the MTs from a pixelated dataset. We apply a linear RSD operator to simulated isotropic Gaussian density fields and discuss how it affects the elements of the MTs in section 5.5. We also explain how this method probes the anisotropy generated by the action of the linear RSD operator and hence can be used to constrain the RSD parameter from observations.

## 5.2 Minkowski Tensors in 3D

In this work, we use the rank two MTs which can be defined as [78],

$$W_0^{2,0} \equiv A_0 \int_Q \vec{x}^{\,2}\, \mathrm{d}V \tag{5.1}$$

$$W_t^{r,s} \equiv A_t \int_{\partial Q} G_t\ \vec{x}^{\,r} \otimes \hat{n}^{\,s}\, \mathrm{d}A \tag{5.2}$$

where $t$=1,2,3 and $(r, s)$=(2,0), (1,1) or (0,2). $\vec{x}$ and $\hat{n}$ are respectively the position vector and the unit normal vector to the bounding surface. $G_1 = 1$, $G_2 = (\kappa_1 + \kappa_2)/2$ and $G_3 = \kappa_1 \cdot \kappa_2$, where $\kappa_1$ and $\kappa_2$ are the principle curvatures of the bounding surface for each point. $\otimes$ denotes the symmetric tensor product of two vector quantities and is defined as $\left(\vec{A} \otimes \vec{B}\right)_{ij} = \frac{1}{2}\left(A_i B_j + A_j B_i\right)$. $\vec{x}^{\,r}$ represents the $n$-fold symmteric product of $\vec{x}$ with itslef and similarly for $\hat{n}^{\,s}$. $A_t$ is the normalization constant which is chosen so as to match the scalar MFs. $A_0 = 1/V$, $A_1 = 1/6V$ and $A_2 = 1/3\pi V$. $Q$ represents the volume of the excursion set and $\mathrm{d}V$ denotes the volume element in it, while $\partial Q$ represents the area binding the region and $\mathrm{d}A$ represents the area element on it.

The Eqns. 5.1, 5.2 give a complete set of $3 \times 3$ matrices that can be constructed from $\vec{x}$ and $\hat{n}$ integrated over $Q$ and $\partial Q$. However, not all MTs defined this way are linearly independent. The six linearly independent MTs are: $W_0^{2,0}$, $W_1^{2,0}$, $W_2^{2,0}$, $W_3^{2,0}$, $W_1^{0,2}$ and $W_2^{0,2}$. From these six MTs, only $W_1^{0,2}$ and $W_2^{0,2}$ are translation invariant and we will focus on these two for this work. They can be given by,

$$W_1^{0,2} = \frac{1}{6\,V} \int_{\partial Q} \hat{n}^2\, \mathrm{d}A \tag{5.3}$$

$$W_2^{0,2} = \frac{1}{3\pi\, V} \int_{\partial Q} G_2\, \hat{n}^2\, \mathrm{d}A \tag{5.4}$$

$W_1^{0,2}$ and $W_2^{0,2}$ computed from a given random field can give us useful information about the statistical properties of the field. In the next section, we compute the ensemble average of $W_1^{0,2}$ and $W_2^{0,2}$ for an isotropic Gaussian random field in three dimensions.

## 5.3 Ensemble average for an isotropic Gaussian field

For a smooth isotropic Gaussian random field $u$ in three dimensions, let $\nu$ denote the threshold which defines the boundary $\partial Q$ of the excursion set. In order to analytically perform the integration for $W_1^{0,2}$ and $W_2^{0,2}$, we write down the respective expressions in terms of the field and its first and second order derivatives, $u_i$ and $u_{ij}$. The subscripts $i, j$ represent differentiation with respect to the coordinates $x_i, x_j$ and run over the range $1 \leq i, j \leq 3$. The unit normal vector to the iso-density surface bounnding the excursion set is orthogonal to the surface and can be given as, $\hat{n} = \nabla u / |\nabla u|$. By using a delta function, $\delta(u - \nu)$, the area integrals can be transformed into volume integrals to give,

$$W_1^{0,2} = A_1 \int \mathrm{d}V \, \delta(u - \nu) \, \frac{1}{|\nabla u|} \, \mathcal{M} \tag{5.5}$$

$$W_2^{0,2} = A_1 \int \mathrm{d}V \, \delta(u - \nu) \, \frac{G_2}{|\nabla u|} \, \mathcal{M} \tag{5.6}$$

where the matrix $\mathcal{M}$ can be given as,

$$\mathcal{M} = \begin{pmatrix} u_1^2 & u_1 u_2 & u_1 u_3 \\ u_1 u_2 & u_2^2 & u_2 u_3 \\ u_1 u_3 & u_2 u_3 & u_3^2 \end{pmatrix} \tag{5.7}$$

For a given surface, the mean curvature $G_2$ is related to the unit normal vector to the surface as,

$$G_2 = -\frac{1}{2} \nabla \cdot \hat{n} \tag{5.8}$$

$G_2$ can be expressed in terms of the field derivatives as,

$$G_2 = \frac{1}{2 \left|\nabla u\right|^3} \left[ 2 \left( u_1 u_2 u_{12} + u_2 u_3 u_{23} + u_1 u_3 u_{13} \right) - \left( u_1^2 (u_{22} + u_{23}) + u_2^2 (u_{11} + u_{33}) + u_3^2 (u_{11} + u_{22}) \right) \right] \tag{5.9}$$

We define the quantities $\sigma_0$ and $\sigma_1$ as,

$$\sigma_0^2 \equiv \langle u \rangle^2 \tag{5.10}$$

$$\sigma_1^2 \equiv \langle \nabla u \rangle^2 \tag{5.11}$$

The non-zero correlations which contain the second order field derivatives are,

$$\begin{aligned} \langle u_{ii} u_{ii} \rangle &\equiv c, \qquad \langle u_{ij} u_{ij} \rangle_{i \neq j} \equiv s, \\ \langle u_{ii} u_{jj} \rangle_{i \neq j} &\equiv q, \end{aligned} \tag{5.12}$$

This gives us a ten component column vector $\vec{X} = u, u_1, u_2, u_3, u_{11}, u_{22}, u_{33}, u_{12}, u_{23}, u_{13}$ with a joint probability distribution having the form,

$$P(\vec{X}) = \frac{1}{\sqrt{(2\pi)^{10} \mathbf{Det} \Sigma}} \exp\left( -\frac{1}{2} \vec{X}^T \, \Sigma^{-1} \vec{X} \right) \tag{5.13}$$

$\Sigma$ denotes the covariance matrix $\Sigma \equiv \vec{X} \vec{X}^T$ and is explicitly given in [90]. The ensemble expectation values of $W_1^{0,2}$ and $W_2^{0,2}$ are then given as,

$$\begin{aligned} \left\langle W_1^{0,2}(\nu) \right\rangle &= A_1 \int \mathrm{d}\vec{X} \int \mathrm{d}V \, P(\vec{X}) \, \delta(u - \nu) \, \tfrac{1}{|\nabla u|} \, \mathcal{M}, \\ \left\langle W_2^{0,2}(\nu) \right\rangle &= A_2 \int \mathrm{d}\vec{X} \int \mathrm{d}V \, P(\vec{X}) \, \delta(u - \nu) \, \tfrac{G_2}{|\nabla u|} \, \mathcal{M}, \end{aligned} \tag{5.14}$$

As the volume integrals and the $\vec{X}$ integrals commute, we can interchange the order and do the $\vec{X}$ integration first. This gives us the ensemble expectation values per unit volume,

$$\begin{aligned} \left\langle W_1^{0,2}(\nu) \right\rangle &= \tfrac{\sigma_1}{9\sqrt{3}\,\pi\,\sigma_0} \, e^{-\nu^2/2} \, \mathcal{I} = \tfrac{\langle W_1 \rangle}{3} \, \mathcal{I} \\ \left\langle W_2^{0,2}(\nu) \right\rangle &= \tfrac{\sigma_1^2}{27\,\pi\,\sqrt{2\pi}\,\sigma_0^2} \, \nu \, e^{-\nu^2/2} \, \mathcal{I} = \tfrac{\langle W_2 \rangle}{3} \, \mathcal{I} \end{aligned} \tag{5.15}$$

where $\mathcal{I}$ is the identity matrix and $W_1$ and $W_2$ are the usual scalar MFs defineds as,

$$\begin{aligned} W_1 &= \tfrac{1}{6\,V} \int_{\partial Q} \mathrm{d}A, \\ W_2 &= \tfrac{1}{3\,\pi\,V} \int_{\partial Q} G_2 \, \mathrm{d}A \end{aligned} \tag{5.16}$$

Information on the Gaussian nature of the field is contained in the amplitude of the expectation values, while information on the isotropy of the field is carried by the identity matrix. We can extract information directly from the components of $W_1^{0,2}$ and $W_2^{0,2}$ or from their eigenvalues and eigenvectors. If the field is anisotropic, then the eigenvalues will not be equal, independent of the choice of coordinate system.

## 5.4 Numerical estimation from a discretely sampled field

In this section we estimate the MT statistics from a discretely sampled density field. Two methods that can be used for the numerical estimation of the MTs for three dimensional fields are discussed below.

### 5.4.1 Marching Tetrahedra method

The details of the method of surface generation and computation of MTs from these surfaces are given in [1] [90]. First, discrete random fields, are generated in Fourier space based on a linear ΛCDM matter spectrum with fiducial cosmological parameter values.These fields are smoothed with a Gaussian kernel and then converted to real space to give three dimensional density fields $\delta_{i,j,k}$. $i, j, k$ denote the coordinates of the pixel on a regular lattice with side length $N_{side}$ such that, $1 \leq i, j, k \leq N_{side}$. The fields are normalized by the Root Mean Square (RMS) fluctuation of $\delta_{i,j,k}$ within the box, $\sigma_0$. These fields are used to generate triangulated surfaces of constant density, $\delta = \nu$ by using the marching tetrahedra method [91]. Points on the edges of the tetrahedra with density $\delta = \nu$ are obtained by interpolating the density field linearly and generate a triangulated surface from these points. The scalar MFs and the MTs can then be computed from the iso-density surfaces thus obtained by using the discretized approximations given in [78].

In [90], we have tested this method on an isotropic Gaussian field. We have generated a density field with $N_{side} = 512$ using the method described above and smoothed the field with a Gaussian kernel, $W(kR_G) = e^{-k^2 R_G^2/4}$, where $R_G = 20h^{-1}Mpc$. The field threshold $\nu$ is varied from -3 to +3 in N=40 equi-spaced steps. For each threshold, we generate a triangulated iso-density surface consisting of pixels that satisfy the condition $\delta_{i,j,k} > \nu$ and this surface defines the excursion set. We then numerically estimate the scalar MFs and MTs from these surfaces. We compute the mean and error bars for $W_1^{0,2}$ and $W_2^{0,2}$ numerically from $N_{real} = 50$ realizations and compare them with the theoretical expectation values for an isotropic Gaussian field. We find excellent agreement ($< 1\%$) between the theoretical expectation values and the MTs estimated numerically using this method.

[1] This numerical calculation using the marching tetrahedra method is part of the publication, but is not a part of my thesis work

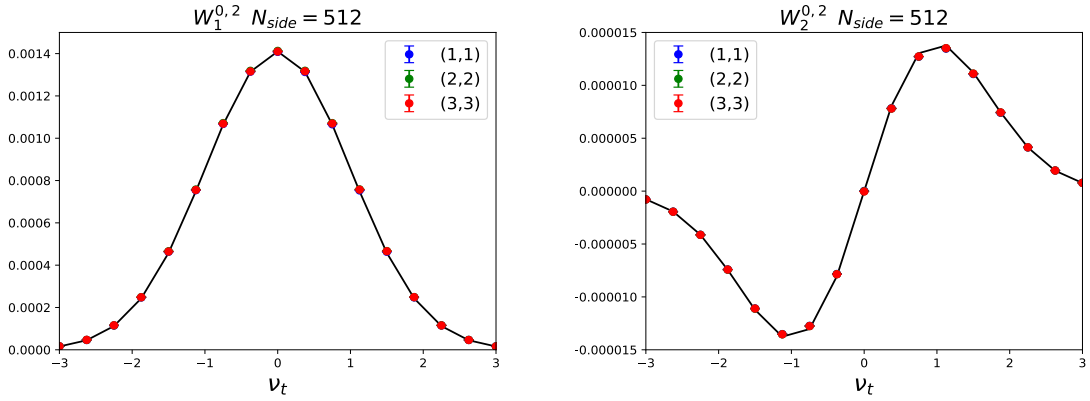


Figure 5.1: MTs estimated for an isotropic Gaussian field using the semi-analytic method. *Left panel*: Diagonal elements of $W_1^{0,2}$ represented by the blue, green and red dots and the theoretical expectation values represented by the black line. The blue, green and red points overlap leading to only the red points being visible. *Right panel*: Same as the left panel, but for $W_2^{0,2}$.

### 5.4.2 Semi-analytic method

Additionally, we have developed a semi-analytic code to estimate the Minkowski Tensors for a discretely sampled density field in three dimensions. As in section 5.4.1, we generate isotropic Gaussian fields in fourier space and then smooth them with a Gaussian kernel and convert them to get three dimensional isotropic Gaussian fields, $\delta_{i,j,k}$, in real space. From each field, the mean is subtracted and then the field values are normalized by the standard deviation, to give fields with zero mean and unit standard deviation. For each realization, we vary the field threshold from -3 to +3 and estimate $W_1^{0,2}$ and $W_2^{0,2}$ using Eqns. 5.5 and 5.6.The field derivatives and second order derivatives are computed in real space for each pixel, by using the difference in the field values of neighbouring pixels in the respective directions. The quantities $\nabla u$ and $G_2$ can be computed from the first and second order field derivatives. Applying the same idea as in [57], for each threshold $\nu$, we approximate the $\delta$-function for the case of discretely sampled fields as,

$$\delta(u - \nu) = \frac{1}{\Delta\nu_t} \tag{5.17}$$

when the field value $u$ lies between $\nu + \Delta\nu$ and $\nu - \Delta\nu$, where $\Delta\nu$ is the threshold bin size.

We have applied our method to simulations of isotropic Gaussian density fields in three dimensions with $N_{side} = 512$ and $R_G = 20h^{-1}Mpc$ generated using the $\Lambda$CDM linear matter power spectrum. We generated 50 simulations and estimated the mean and standard

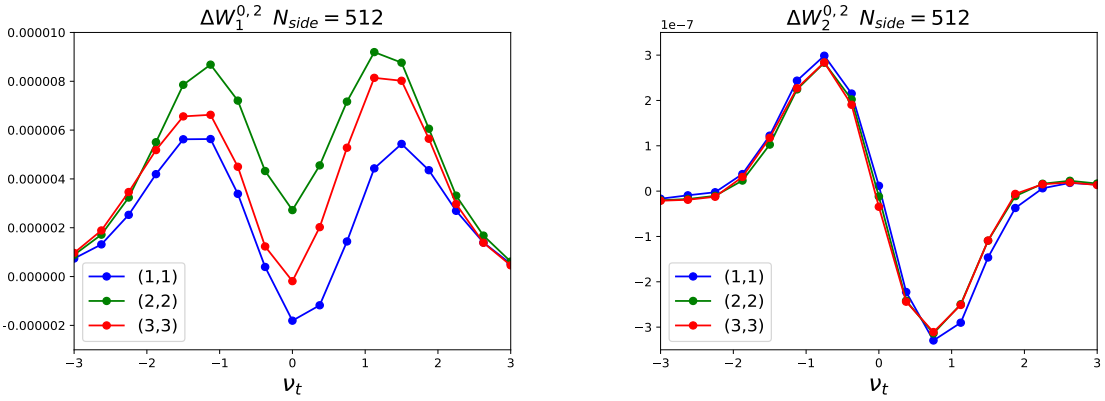


Figure 5.2: Numerical error in the MTs estimated for an isotropic Gaussian field using the semi-analytic method. *Left panel*: Diagonal elements of $\Delta W_1^{0,2}$ from Eqn. 5.18 represented by the blue, green and red lines. *Right panel*: Same as the left panel, but for $\Delta W_2^{0,2}$ from Eqn. 5.19.

deviations of $W_1^{0,2}$ and $W_2^{0,2}$, which are displayed in Fig. 5.1. The diagonal elements (1,1), (2,2) and (3,3) of $W_1^{0,2}$ are represented by the blue, green and red dots respectively in the left panel, while the theoretical expectation values for an isotropic Gaussian field are represented by the black line. In the right panel of Fig. 5.1, the diagonal elements (1,1), (2,2) and (3,3) of $W_2^{0,2}$ are represented by the blue, green and red dots respectively. Again, the black line represents the theoretical expectation values for an isotropic Gaussian field. To quantify the numerical error in the MTs estimated using our method, we define the following quantities,

$$\Delta W_1^{0,2}(\nu_t) = W_1^{0,2}(\nu_t) - W_1^{(G)0,2}(\nu_t), \tag{5.18}$$

$$\Delta W_2^{0,2}(\nu_t) = W_2^{0,2}(\nu_t) - W_2^{(G)0,2}(\nu_t). \tag{5.19}$$

$W_1^{0,2}(\nu_t)$ and $W_2^{0,2}(\nu_t)$ represent the MTs estimated using our method, $W_1^{(G)0,2}(\nu_t)$ and $W_2^{(G)0,2}(\nu_t)$ represent the respective expectation values for an isotropic Gaussian field and $\Delta W_1^{0,2}(\nu_t)$ and $\Delta W_2^{0,2}(\nu_t)$ represent the corresponding numerical errors in the estimated MTs. We have computed $\Delta W_1^{0,2}(\nu_t)$ and $\Delta W_2^{0,2}(\nu_t)$ based on the mean MTs estimated from 50 simulations of $N_{side}$=512 and the results are displayed in Fig. 5.2. In the left panel, the diagonal elements (1,1), (2,2) and (3,3) of $\Delta W_1^{0,2}(\nu_t)$ are represented by the blue, green and red lines respectively. The right panel shows the diagonal elements (1,1), (2,2) and (3,3) of $\Delta W_2^{0,2}(\nu_t)$ which are again represented by the blue, green and red lines respectively.

We find that the MTs estimated using our method for isotropic Gaussian fields are

consistent with the corresponding theoretical expectation values at the subpercent level. This work is part of my thesis and is currently in progress.

## 5.5 Effect of anisotropy on the Minkowski Tensors

For isotropic Gaussian random fields, the MTs we discussed here are proportional to the product of the scalar MFs and the identity matrix. In this section, we study the effect of anisotropy on these statistics. We first generate an isotropic Gaussian field $\delta_{i,j,k}$ from a linear $\Lambda$CDM matter power spectrum using fiducial parameter values. We arbitrarily take the $x_3$-axis as the line of sight and apply a linear RSD operator. This way we generate 50 realizations of an anisotropic Gaussian field from the same $\Lambda$CDM matter power spectrum given in section 5.4. The following transformation is applied to an isotropic density field in fourier space to get an anisotropic redshift space distorted field,

$$\delta^{(rsd)}(\vec{k}) = b\,(1 + \Upsilon\mu_{\vec{k}}^2)\,\delta(\vec{k}) \tag{5.20}$$

where $\mu_{\vec{k}}^2 = k_{x_3}^2/k^2$ and the RSD parameter is $\Upsilon = f/b$. $f \approx \Omega_m^{6/11}$ is the growth parameter and $b$ is the bias. We have used the plane-parallel approximation which reduces the RSD effect to the Kaiser effect that corresponds to a shift in the amplitude in the Fourier space by an amount $1 + \Upsilon\mu_{\vec{k}}^2$. We then smooth the field in the Fourier space with a Gaussian beam of width $R_G = 20h^{-1}Mpc$. The MTs are then computed for both the isotropic field, $\Upsilon = 0$, and the redshift space distorted field, $\Upsilon \neq 0$. We set $b = 1$ and $\Upsilon = \Omega_m^{6/11}$ because we use the matter density field directly instead of a biased tracer such as the galaxy or halos. Since $\Upsilon$ is dependent on redshift, the resultant $W_1^{0,2}$ and $W_2^{0,2}$ matrices will also depend on the redshift. Here we generate the fields at redshift zero.

We find that the effect of RSD is to introduce a constant shift in the relative amplitude of the diagonal elements. The diagonal elements of the matrices are no longer equal and this signal is more pronounced in $W_1^{0,2}$. In our analysis, we have chosen the coordinate system such that the $x_3$-axis is along the line of sight. For a random choice of coordinates, the matrices should be first diagonalized and the effect of RSD would be to give unequal eigenvalues for the matrices. Based on our findings, we can say that the RSD parameter $\Upsilon = f/b$ can be constrained by the measurements of the diagonal elements of $W_1^{0,2}$ and $W_2^{0,2}$.

## 5.6 Summary

In this work, we have introduced MTs for three dimensional fields. We have calculated the ensemble expectation values of the rank two translation independent MTs $W_1^{0,2}$ and $W_2^{0,2}$ for isotropic Gaussian random fields. An algorithm for generating closed iso-density surfaces to extract these statistics from a discretely sampled field is also provided. The MTs estimated numerically using our method show excellent agreement with the theoretical expectation values for the same quantities for isotropic Gaussian fields. For such fields, the MTs are proportional to the scalar MFs and the identity matrix. Any departure from Gaussianity or isotropy can modify $W_1^{0,2}$ and $W_2^{0,2}$ to give non-zero off-diagonal components or unequal diagonal components.

We generate simulated RSD fields by applying a linear RSD operator to isotropic Gaussian fields generated from a linear $\Lambda$CDM matter power spectrum and apply our numerical algorithm to the resultant fields. RSD distorts the shapes of the connected regions and holes along the line of sight and leads to a preferred direction in the normals to the iso-density surfaces. Using our method, we find that RSD modifies the amplitudes of $\Delta W_1^{0,2}$ and $\Delta W_2^{0,2}$ by $\approx 10\%$ as compared to the corresponding isotropic fields. This amplitude shift can be used to constrain the RSD parameter $\Upsilon = f/b$.

In this work, we have used linear density fields and the Kaiser approximation which is a result of the coherent infall of mass into over dense regions. It is expected that the these statistics can also probe the non-linear anisotropies resulting from the Finger of God effect. However, non-linear gravitational collapse is statistically isotropic on all scales and thus we expect that $W_1^{0,2}$ and $W_2^{0,2}$ will not be sensitive to it. The eigenvalues of these MTs provide an independent measure of the level of non-Gaussianity in the field and carry information complementary to the scalar MFs.

# 6

# CONSTRAINING SPACETIME NONCOMMUTATIVITY WITH CMB OBSERVATIONS

## 6.1 Introduction

This chapter covers the second part of our work, testing the prediction of noncommutativity of spacetime, using cosmological data. Noncommutativity of spacetime is a common prediction of many quantum theories of gravity. If true, the effects on noncommutative spacetime would be relevant at length scales that are comparable to the Planck length scale. In noncommutative spacetime, the power spectrum of the primordial density perturbations gets modified. The primordial density perturbations give rise to the matter distribution and the CMB fields that we observe today. Hence a modification of the primordial power spectrum, in turn leads to a modification of the power spectrum of the density distribution and CMB fields. We analyze the observed CMB fields and search for signatures of spacetime noncommutativity.

In order to understand how the information on spacetime noncommutativity, contained in the primordial perturbations is carried over to the CMB fields, we review the inflationary scenario. In the simplest model, inflation arises due to the evolution of a scalar field, the so-called inflaton field. The initial seeds of gravitational potential wells around which matter could cluster and form structures, is provided by the quantum flucuations of the inflaton field. If the prediciton of noncommutative spacetime is correct, then the signature of non-

commutativity would be present in the statistical properties of these quantum fluctuations. As described in Section 2.2.2, the Universe expands rapidly during the Inflationary phase and as a result, tiny regions of space expand to cosmological sizes in an extremely short amount of time. This leaves signatures of the small scale physics, such as noncommutative spacetime, which is relevant for the tiny regions, on the large scale observables such as the CMB fields and the distribution of matter in our Universe. Thus inflation gives us an opportunity to test the prediction of spacetime noncommutativity, using the density distribution and CMB fields.

In the literature, there have been many studies [18, 19, 24, 92–106] probing the effect of spacetime noncommutativity on inflation and signatures in the CMB. A derivation of the modification of the CMB angular power spectrum due to the noncommutativity of spacetime was done in [18]. The noncommutativity parameter in [18], was constrained using data from WMAP [107–109], ACBAR [110–112] and CBI [113–117], in [19].

We follow a methodology similar to that of [19] and analyze the effect of spacetime noncommutativity on the angular power spectrum of the CMB temperature fluctuations. First we the publicly available package CAMB [47, 48] to compute the theoretical CMB angular power spectrum of temperature fluctuations for some non-zero values of the noncommutativity parameter. We find that the CMB power spectrum is most sensitive to the noncommutativity parameter in the range of scales probed by the *Planck* mission. Further, we study the effect of spacetime noncommutativity on the angular power spectrum of the $E$ mode of CMB polarization. We find that the effect of the noncommutativity parameter is much weaker on the $E$ mode power spectrum, than on the temperature fluctuations. Hence, we conclude that the *Planck* temperature fluctuations data is best suited to constrain the noncommutativity parameter.

We use data from *Planck* [31], Baryon Acoustic Oscillations (BAO) from SDSS-DR9 [32, 33] and 6dFGS [34], and BICEP2 CMB polarization data [35] , to constrain the spacetime noncommutativity parameter, by performing Markov Chain Monte Carlo (MCMC) anaylsis. We obtain a constraint on the noncommutativity parameter, that is tighter by about a factor of 2 over the previous constraint obtained in [19]. *Planck* has higher resolution and accuracy compared to WMAP, ACBAR and CBI and this is what leads to the improvement in the constraint.

## 6.2 Noncommutativity parameter

Here we go through the basic equations of noncommutative spacetime and how it affects the angular power spectrum of the CMB temperature fluctuations and *E* mode of polarization. We will follow the same formulation, as given in [18, 19]. In noncommutative spacetime, the coordinate operators, $\hat{x^\mu}$, do not commute and the commutator is given as follows,

$$\left[\hat{x^\mu}, \hat{x^\nu}\right] = i\theta^{\mu,\nu}, \tag{6.1}$$

where $\theta^{\mu,\nu}$ is a constant antisymmetric matrix with dimension $L^2$. Since this is an application to cosmology, it is natural to choose a coordinate system where the time coordinate represents the proper time for an observer in a galaxy and the physical coordinates measure distance in such spatial slices. On the right hand side of Eq. 6.1, we have the physical $\theta^{\mu,\nu}$, which remains constant throughout the evolution of the Universe.

In conformal coordinates, Eq. 6.1 retains its form, while $x^\mu$ now represent coordinates in the conformal frame. However, $\theta^{\mu,\nu}$ would not be constant in time and $\theta^{\mu,\nu}$ in physical coordinates would be related to that in conformal coordinates as follows,

$$\begin{aligned} \theta^{0i,ph} &= a(t)\,\theta^{0i,co}(t) \\ \theta^{ij,ph} &= a(t)\,\theta^{ij,co}(t) \end{aligned} \tag{6.2}$$

where, the superscripts "ph" and "co" represent the physical and the conformal frames respectively, while $a(t)$ represents the scale factor of the expansion of the Universe. In this work, we perform all our calculations in the conformal frame and in the end, we convert the resultant constraint to the physical frame. To simply the notation, we will use, $\theta^{\mu\nu}$ when we actually mean, $\theta^{\mu\nu,co}(t)$.

If spacetime is noncommutative, then that leads to a deformation of the fields. Let $\phi_0$ denote a field in commutative spacetime and let $\phi_\theta$ denote the corresponding deformed field in noncommutative spacetime. In our case, the field in consideration is the field of scalar perturbations generated during inflation. The deformation of the field due to spacetime noncommutativity, leads to a modified power spectrum, $P_{\Phi_\theta}(\mathbf{k})$, which is related to the usual power spectrum in commutative spacetime, $P_{\Phi_0}(k)$, as given by [18],

$$P_{\Phi_\theta}(\mathbf{k}) = P_{\Phi_0}(k)\cosh\left(H\vec{\theta}^0 \cdot \mathbf{k}\right) \tag{6.3}$$

$P_{\Phi_0}(k)$ is the usual direction independent power spectrum in commutative spacetime. It is given by,

$$P_{\Phi_0}(k) = \frac{A_s}{k^3}\left(\frac{k}{k_0}\right)^{n_s-1} \tag{6.4}$$

where, $A_s$ is the amplitude of scalar perturbations, $n_s$ is the scalar spectral index and $k_0$ is a pivot scale that we can choose. The modified angular power spectrum of the CMB temperature fluctuations in noncommutative spacetime is then given by [19],

$$C_\ell^{TT} = \int dk\, k^2\, P_{\Phi_0}(k)\, \left|\Delta_\ell^T(k)\right|^2\, i_0(\theta H k) \tag{6.5}$$

where, $i_0$ is the modified spherical bessel function of the first kind. It is given by, $i_0(x) = \frac{\sinh(x)}{x}$. $\left|\Delta_l^T(k)\right|$ is the transfer function for the CMB temperature fluctuations. It contains information about the physical processes that affect the evolution of the fluctuations from the epoch of last scattering till the time of observation. In this work, we assume that spacetime noncommutativity does not affect $\left|\Delta_l^T(k)\right|$, since $\left|\Delta_l^T(k)\right|$ is relevant at scales much larger than the noncommutativity length scale.

The polarization degrees of freedom of the CMB photons can be decomposed into the *E* and *B* modes. The *E* modes represent the curl free component while the *B* modes represent the divergence free component. In a way similar to the temperature fluctuations, the modified angular power spectrum of the *E* mode of CMB polarization, $C_\ell^{EE}$, can also be derived. It is given by,

$$C_\ell^{EE} = \int dk\, k^2\, P_{\Phi_0}(k)\, \left|\Delta_\ell^E(k)\right|^2\, i_0(\theta H k) \tag{6.6}$$

where, $\left|\Delta_l^E(k)\right|$ is the transfer function for the *E* mode of CMB polarization.

## 6.3 Effect of spacetime noncommutativity on the CMB power spectrum

In this section, we estimate the effect of spacetime noncommutativity on the angular power spectrum of CMB temperature and *E* mode fields. For our calculations, we will work with the quantity $D_\ell^i$, where $i$ refers to $TT$ or $EE$. $D_\ell^i$ is related to $C_\ell^i$ as,

$$D_\ell^i \equiv \frac{\ell(\ell+1)}{2\pi} C_\ell^i \tag{6.7}$$

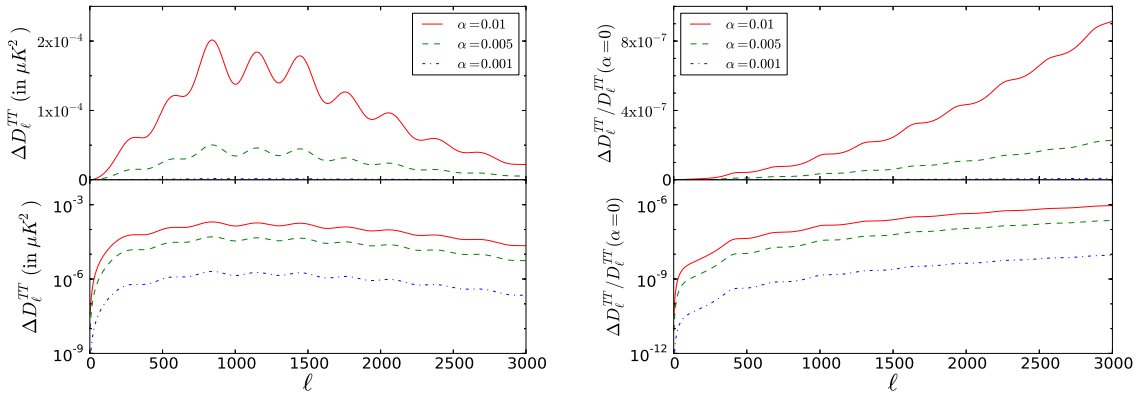


Figure 6.1: Comparison of $\Delta D_\ell^{TT}(\alpha)$ and $\Delta D_\ell^{TT}/D_\ell^{TT}(\alpha)$ values computed for different values of $\alpha$ with linear and log scale on the y axis.

We denote the quantity $\theta H$ by $\alpha$ and study the variation in $D_\ell^i$ with respect to $\alpha$. In this work, the publicly available code CAMB [47,48] was used to compute the $D_\ell^i$. CAMB solves the Boltzman equation for the early Universe to obtain the transfer functions, $\Delta_\ell^i$, for the CMB temperature fluctuations, *E* and *B* modes of polarization. Then it performs the integral over $k$ in Eq. (6.5) and (6.6) to obtain the $D_\ell^i$s. For our work, in order to calculate the angular power spectrum in noncommutative spacetime, we modify CAMB to incorporate the factor of $i_0$ in the expression for the primordial power spectrum. To see how $D_\ell^i$ changes with $\alpha$, we first calculate $D_\ell^i(\alpha)$ for different values of $\alpha$ and the we compute the difference, $\Delta D_\ell^i(\alpha) = D_\ell^i(\alpha) - D_\ell^i(0)$. We systematically change $\alpha$ and study how $\Delta D_\ell^i(\alpha)$ changes.

A comparison of $\Delta D_\ell^{TT}(\alpha)$ for different values of $\alpha$ is plotted in Fig. 6.1. The argument of $i_0$ in Eq. (6.5) and (6.6) is a dimensionless quantity. We have taken $\alpha$ in units of Mpc since the unit of $k$ used in CAMB is Mpc$^{-1}$. For our work, we have used the *Planck* best-fit values for the $\Lambda$CDM cosmological parameters [31]. $i_0(x)$ is a monotonically increasing function of $x$ that goes to one as $x \to 0$. Hence, for larger values of $\alpha$, we find an overall increase in the amplitude of $C_\ell$. As seen in the left panel of Fig. 6.1, the difference between the $D_\ell^{TT}$s for various values of $\alpha$, is the largest for the range $\ell < 3000$. This is the range of multipoles probed by the *Planck* mission and so *Planck* data is the most suitable for constraining $\alpha$ from CMB observations. We find that with decreasing $\alpha$, there is a sharp decrease in the amplitude of $\Delta D_\ell^{TT}(\alpha)$. The right panel of Fig. 6.1 shows a comparison of $\Delta D_\ell^{TT}/D_\ell^{TT}(\alpha)$ with linear and log scale on the y axis. This plot demonstrates the effect of the $i_0$ factor on the $D_\ell^{TT}(\alpha)$ calculations.

In figure 6.2, we have shown the effect of $\alpha$ on the computation of $\Delta D_\ell^{EE}(\alpha)$ and

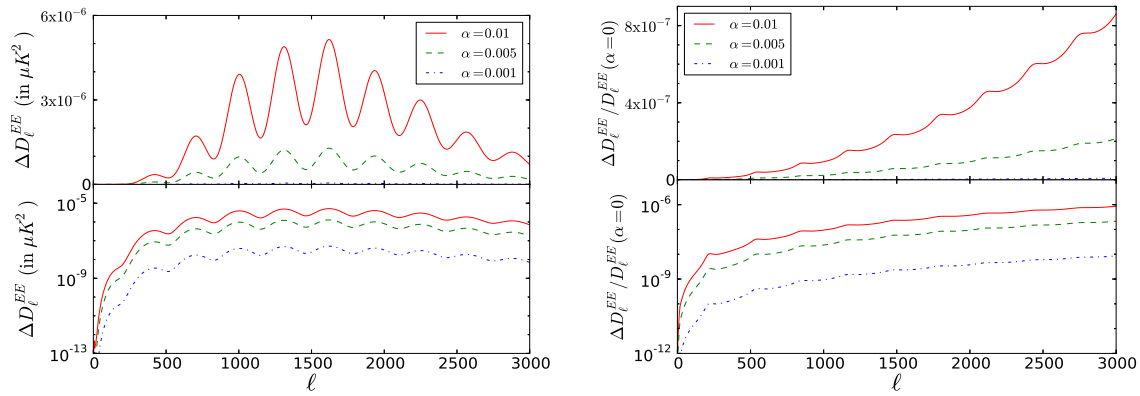


Figure 6.2: Comparison of $\Delta D_\ell^{EE}(\alpha)$ and $\Delta D_\ell^{EE}/D_\ell^{EE}(\alpha)$ values computed for different values of $\alpha$ with linear and log scale on the y axis.

$\Delta D_\ell^{EE}/D_\ell^{EE}(\alpha)$. Both the panels here are similar to those in Fig. 6.1. The amplitude of $\Delta D_\ell^{EE}(\alpha)$ is about two orders of magnitude smaller than that of $\Delta D_\ell^{TT}(\alpha)$ for the corresponding values of $\alpha$, as seen in the left panel of Fig. 6.2. We find that the ratio $\Delta D_\ell^{EE}/D_\ell^{EE}(\alpha)$ has values similar to those of $\Delta D_\ell^{TT}/D_\ell^{TT}(\alpha)$ for the same values of $\alpha$. Based on this figure, we conclude that CMB *E* mode data can not significantly improve upon the constraint on $\alpha$ obtained from CMB temperature data, even though polarization provides independent information about the properties of the Universe.

## 6.4 Method and data

In this section, we compare the standard $\Lambda$CDM cosmological model with noncommutative spacetime, with CMB temperature fluctuations data from *Planck* [31]. Additionally, we also use BAO data from SDSS [32, 33] and 6DFGS [34], and CMB polarization data from BICEP2 [35]. In this work, the baryon density $\Omega_b h^2$, cold dark matter density $\Omega_c h^2$, the Hubble parameter $H_0$, optical depth of reionization $\tau$, the amplitude $A_s$ and spectral index $n_s$ of the primordial scalar perturbations are the cosmological parameters used. Additionally, we have the spacetime noncommutativity parameter $\alpha \equiv \theta H$, for a total of seven parameters.

To constrain $\alpha$, we perform a Bayesian statistical inference analysis of the data using the publicly available MCMC package COSMOMC [48, 49] for cosmological parameter estimation. A modified version of CAMB as described in section 6.3 was used for calculating the theoretical angular power spectra for the temperature fluctuations and *E* mode of CMB polarization. These spectra go in as inputs for the likelihood analysis. To test

the convergence of the generated Markov chains, we use the Gelman-Rubin convergence criterion $R - 1 < 0.02$. $R$ denotes the ratio of the variance of chain means to the mean of chain variances. For the six standard model parameters, we use the default flat priors given in COSMOMC. We choose a flat prior for $\alpha$ with an upper limit value of $0.1$ and a lower limit value of $10^{-8}$. We set the upper limit to have a range wide enough to accommodate the constraint obtained by [19]. The lower limit was chosen so that the results obtained, from several runs of COSMOMC with progressively smaller values of $\alpha$, are stable. We run COSMOMC for different combinations of the observational data sets and present here the results for (a) *Planck* data alone, (b) *Planck* + BAO data and (c) *Planck* + BAO + BICEP2 data. For *Planck* data, $\ell_{max} = 2479$ is the largest multipole.

## 6.5 Results

### 6.5.1 Best fit values and parameter constraints

First we shall describe the result obtained using *Planck* data alone. The one-dimensional mean (dashed lines) and the marginalized (solid lines) likelihood curves for $\alpha$ are shown in Fig. 6.3. We find that $\alpha$ is constrained to have only those values which fall below a certain upper bound. A comparison of the best fit values and 2-$\sigma$ limits of the $\Lambda$CDM parameters in the case of commutative and noncommutative spacetime are shown in Table . We find only marginal changes in the values of the $\Lambda$CDM model parameters when spacetime is taken to be noncommutative. We obtain the upper bounds, $\alpha < 0.0026$ and $\alpha < 0.0087$ at 1-$\sigma$ and 2-$\sigma$, respectively.

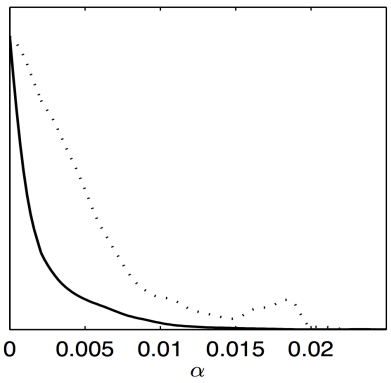


Figure 6.3: The one-dimensional mean (the dashed lines) and marginalized (solid lines) likelihood curves for $\alpha$, obtained using *Planck* data alone.

$i_0$ is a monotonically increasing function and so it is possible that there is a degeneracy between $\alpha$ and $n_s$ and to a mild extent with $H_0$. In order to probe these possible degeneracies, we have computed the 1-$\sigma$ and 2-$\sigma$ two-dimensional joint constraints between these three parameters. These are shown in Fig. 6.4. We find that the degeneracy between these three parameters is very mild and that the strength of the degeneracy is larger for larger $\alpha$ values, as we can see from the 2-$\sigma$ contour.

We repeated the same analysis for noncommutative spacetime with *Planck*+BAO and *Planck*+BAO+BICEP2 datasets. The mean values and 2-$\sigma$ error bars for the cosmological parameters and the 1-$\sigma$ and 2-$\sigma$ upper limits for $\alpha$ are shown in Table 6.2. We find marginal shifts in the 1-$\sigma$ and 2-$\sigma$ upper bounds for $\alpha$ on including the BAO and BICEP2 datasets. Including the BICEP2 data in the analysis leads to slightly tighter constraints on $\alpha$.

### 6.5.2 Constraint on the physical noncommutativity parameter

In the previous section, we obtained the constraints on $\alpha$ using *Planck* data. Here we will convert these into the corresponding 1-$\sigma$ and 2-$\sigma$ constraints on the physical noncommutativity parameter, $\theta^{ph}$. $\alpha$ is related to the noncommutativity parameter in conformal coordinates, $\theta$ as,

| Parameter | *Planck* Commutative spacetime | *Planck* Noncommutative spacetime |
|---|---|---|
| $\Omega_{\rm b}h^2$ | $0.0220\,^{0.0226}_{0.0215}$ | $0.0219\,^{0.0225}_{0.0214}$ |
| $\Omega_{\rm c}h^2$ | $0.1199\,^{0.1251}_{0.1147}$ | $0.1198\,^{0.1252}_{0.1147}$ |
| $H_0$ | $67.29\,^{69.65}_{64.98}$ | $67.23\,^{69.53}_{64.90}$ |
| $\tau$ | $0.0898\,^{0.1158}_{0.0640}$ | $0.0878\,^{0.1134}_{0.0622}$ |
| $n_s$ | $0.9605\,^{0.9748}_{0.9462}$ | $0.9599\,^{0.9738}_{0.9457}$ |
| $\ln(10^{10}A_s)$ | $3.090\,^{3.139}_{3.043}$ | $3.084\,^{3.134}_{3.036}$ |
| $\alpha \equiv \theta H$ | — | $< 0.0026$ (1-$\sigma$) |
| | — | $< 0.0087$ (2-$\sigma$) |

Table 6.1: The mean values and the 2-$\sigma$ error bars for the $\Lambda$CDM parameters in commutative spacetime and in noncommutative spacetime, obtained using PLANCK data alone. For $\alpha$ we have given the 1-$\sigma$ and 2-$\sigma$ upper bounds. The pivot scale used for $A_s$ is $k = 0.05$ Mpc$^{-1}$.

$$\alpha = H\theta. \tag{6.8}$$

Further, $\theta$ is related to the physical noncommutativity parameter $\theta^{ph}$ as given in Eq. 6.2. Hence, to convert the constraints on $\alpha$ into constraints on $\theta^{ph}$, we must first obtain the constraints on $\theta$ by fixing the value of $H$ during inflation. Denoting the power spectrum of primordial tensor perturbations by $P_T$ and the tensor to scalar ratio $P_T/P_\phi$ by $r$, we use the relation $P_T = (H/2\,\pi)^2$ to obtain,

$$H^2 = (2\pi)^2\, r\, P_\phi. \tag{6.9}$$

We use the best fit value of $A_s$ from the column with noncommutativity spacetime in Table 6.1, along with the 2-$\sigma$ limit $r < 0.11$ from *Planck* [31] in Eq. 6.9 to obtain

$$H < 1.943 \times 10^{-5}\, M_P, \tag{6.10}$$

where $M_P$ is the Planck mass. We take the 1-$\sigma$ limit on $\alpha$ given in the third column of Table 6.1 and obtain the 1-$\sigma$ constraint on $\theta$ to be $\theta < 0.427 \times 10^{-9}$ m$^2$. Similarly, by using the 2-$\sigma$ constraint on $\alpha$, we obtain the 2-$\sigma$ constraint on $\theta$ to be $\theta < 1.406 \times 10^{-9}$ m$^2$.

Next, we will use the value of the cosmological scale factor ,$a$, at the end of inflation,

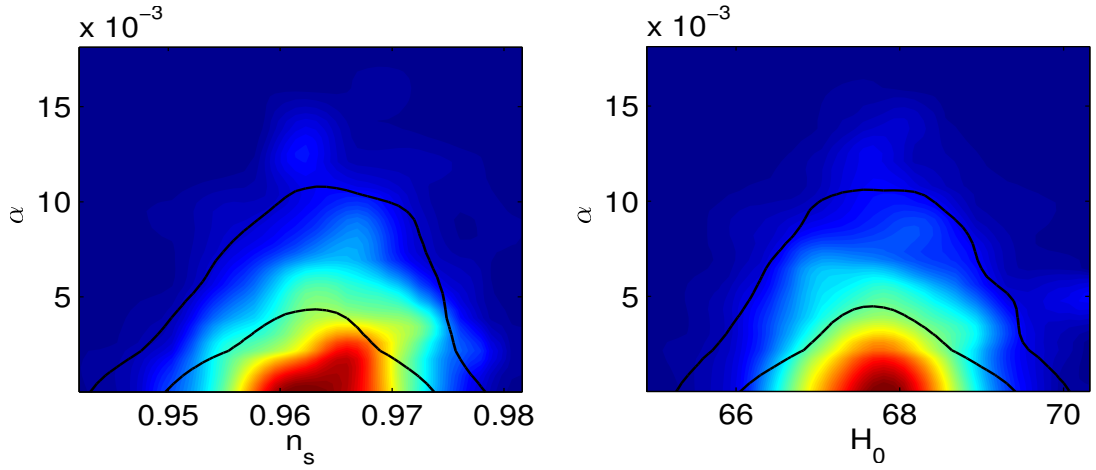


Figure 6.4: The joint two-dimensional constraints at 1-$\sigma$ and 2-$\sigma$ confidence levels on $\alpha$, $n_s$ and $H_0$, obtained using *Planck* data alone.

to obtain constraints on $\theta^{ph}$. If we follow the assumption in [19], that the temperature of reheating of the Universe was close to the grand unified theory energy scale, $10^{16}GeV$, then the scale factor at the end of inflation is $a \approx 10^{-29}$. We use this value of $a$ to obtain the constraint on the physical noncommutativity parameter to be $\sqrt{\theta^{ph}} < 0.653 \times 10^{-19}$m at 1-$\sigma$ and $\sqrt{\theta^{ph}} < 1.186 \times 10^{-19}$m at 2-$\sigma$. The corresponding lower bounds on the noncommutativity energy scale are 18.9764 and 10.4548 TeV at 1-$\sigma$ and 2-$\sigma$ respectively. If the reheating temperature is different, then these numbers will also change. The 1-$\sigma$ constraint that we have obtained on $\theta^{ph}$ is about a factor of two improvement over the constraint obtained in [19].

| Parameter | *Planck* + BAO | *Planck* + BAO + BICEP2 |
|---|---|---|
| $\Omega_{\rm b}h^2$ | $0.0220\,^{0.0225}_{0.0215}$ | $0.0219\,^{0.0224}_{0.0214}$ |
| $\Omega_{\rm cdm}h^2$ | $0.1187\,^{0.1223}_{0.1153}$ | $0.1196\,^{0.1231}_{0.1162}$ |
| $H_0$ | $67.71\,^{66.10}_{69.25}$ | $67.30\,^{68.82}_{65.81}$ |
| $\tau$ | $0.0896\,^{0.1151}_{0.0657}$ | $0.0964\,^{0.1233}_{0.0717}$ |
| $n_s$ | $0.9622\,^{0.9733}_{0.9504}$ | $0.9600\,^{0.9709}_{0.9487}$ |
| $\ln(10^{10}A_s)$ | $3.08\,^{3.13}_{3.03}$ | $3.10\,^{3.15}_{3.05}$ |
| $\alpha \equiv \theta H$ | $< 0.0025$ (1-$\sigma$)<br>$< 0.0083$ (2-$\sigma$) | $< 0.0021$ (1-$\sigma$)<br>$< 0.0074$ (2-$\sigma$) |

Table 6.2: The mean values and the 2-$\sigma$ error bars for the $\Lambda$CDM model parameters in noncommutative spacetime, obtained using *Planck*+BAO and *Planck*+BAO+BICEP2 data sets. We have shown the 1-$\sigma$ and 2-$\sigma$ upper bounds for $\alpha$. The pivot scale used for $A_s$ is again $k = 0.05$ Mpc$^{-1}$.

## 6.6 Summary

In this chapter, we have confronted the prediction of noncommutative spacetime, with observational data from *Planck*, BAO and BICEP2. If spacetime is noncommutative, then the power spectrum of primordial scalar perturbations is modified and this can used to test the prediction. First, we studied the effect of noncommutative spacetime on the theoretical angular power spectrum of CMB temperature fluctuations and the *E* mode of CMB polarization. We find that this effect is most pronounced in the range of multipoles $\ell < 3000$, which is the range probed by *Planck*. Thus we expect *Planck* data to give more stringent constraints than those given by WMAP data. We also find that spacetime noncommutativity has a much weaker effect on the CMB *E* mode than on the CMB temperature fluctuations and hence the constraints will not be improved significantly with the inclusion of *E* mode data.

In order to constrain the spacetime noncommutativity scale, $\theta^{ph}$, we compare the theoretical angular power spectra of CMB temperature fluctuations with those obtained from observations, mainly *Planck* data. We obtain the best fit values of the $\Lambda$CDM cosmological parameters and the spacetime noncommutativity parameter by performing an MCMC likelihood analysis of the data. We find an upper bound $6.23 \times 10^{-20}$m on the value of $\theta^{ph}$ at 1-$\sigma$, which improves upon the previous constraint using WMAP, ACBAR and CBI data, by

a factor of about 2. The higher angular resolution of *Planck* in comparison to WMAP and its higher precision in comparison to ACBAR and CBI is what leads to the improvement in the constraints.

The effect of spacetime noncommutativity on the CMB fields decreases at multipoles higher than 3000 and so we expect that inclusion of CMB data at smaller scales will not significantly improve the constraint. Since the effect on the CMB $E$ mode is much weaker than on the temperature fluctuations, the inclusion of $E$ mode data will also not significantly improve the constraint. Spacetime noncommutativity will aslo affect the power spectrum of the primordial tensor modes [118] and it will show up in the angular power spectrum of the $B$ mode of CMB polarization. We have not included this effect in our analysis. It will not have an impact on our results since BICEP2 data is restricted to lower multipole range where the effect of noncommutative spacetime is negligible. In the future, including high resolution $B$ mode data can potentially improve the constraint on $\theta^{ph}$. However, this is subject to improvements in our ability to disentangle physical effects like the gravitational lensing due to the large scale structure, that are important at the smaller scales.

# 7

# SUMMARY AND FUTURE PROSPECTS

## 7.1 Summary

This thesis presents a test of the assumptions of fundamental physics such a commutativity of spacetime and statistical isotropy, against cosmological data, mostly the CMB temperature fluctuations. The CMB and LSS are important observational tools which allow us to probe the laws of physics that govern our Universe, both at the large and small scales. High precision measurements of the CMB temperature and polaization fields enable us to impose tight constraints on the various proposed models of the Universe. Such studies help us in obtaining a deeper understanding of the Universe. The CMB also facilitates a way to probe physics beyond the standard model by providing useful information on the dark matter and dark energy content of our Universe. In this work, we mostly focus on testing the prediction of noncommutative spacetime and the assumption that our Universe is statistically isotropic, by analyzing the CMB data.

In chapter 1, we present a brief account of the standard hot big bang model of the Universe and discuss some of its limitations. We then introduce the concept of cosmic inflation and discuss how it resolves some of these limitations. Further, we discuss the evolution of the Universe post the inflationary era and the epoch of last scattering. The CMB is relic radiation emitted at the epoch of last scattering which free streamed to us today after travelling for almost the age of the Universe. We explain the importance of CMB in the advancement of physics and its role in constraining the various models of inflation. Further, we discuss some of the key experiments carried out to make measurements of the CMB fields and the features that were found in these observations.

In chapter 2, we discuss the information that is carried by the CMB radiation and its usefulness to physics. We also present the main goals of this work and the problem statements of the research work that I have carried out during my term as a PhD. student. These include testing the commutativity of our spacetime and developing tools for testing the statistical isotropy (SI) of random fields and applying them to CMB data. This chapter also contains an account of the observational data that was used during the course of this work. Further, we also give a brief introduction to some of the key software packages such as HEALPIX, CAMB and COSMOMC that we have used for our analysis.

For testing the SI of CMB data, we use Minkowski Tensors (MTs) which are mathematical quantities which carry information regarding the shape of closed curves. Chapter 3 contains an introduction to Minkowski Tensors in flat 2D space and an explanation as to how they carry isotropy information. By isotropy, we refer to the $m$-fold symmetry of the closed curve, for $m \geq 3$. We discuss the generation of closed curves from random fields by selecting a threshold value to cut off the field. The MT method can then be applied to these closed curves. We also introduce the shape and aligment parameters and discuss a method to use these parameters to probe the isotropy of random fields in flat 2D spaces.

In chapter 4, we discuss the application of the MT method to the CMB fields. The MT definitions carry a position vector term which is not usually well defined on curved spaces, making it difficult to apply the MT method to CMB fields which are defined on the sphere. One way to work around this issue is to stereographically project the fields onto a plane and carry out the analysis on the projected fields. We have discussed the limitations of this method and the importance of computing the MTs directly on the sphere. We generalize the definitions of the MTs to closed curves on the sphere, enabling their direct application to the CMB fields. Further, we apply the MT method to look for violations of SI in the CMB temperature data provided by *Planck*. We find excellent agreement between data and simulations for the SMICA frequency coadded CMB temperature map and the beam convolved maps at all frequencies except the 30 GHz observations. For the 30 GHz band, we find $\approx$ 2-$\sigma$ deviation from SI. We suspect that this mild discrepancy arises from inaccurate estimation of the instrument beam or residual noise at 30 GHz. Further investigation of the instrument beam and residual noise is needed before we can confirm the origin of this discrepancy.

In chapter 5, we present a method to constrain the linear redshift-space distortion parameter by using MTs for density fields in three dimensions. The peculiar velocities of objects in galaxy clusters and super clusters affect the observed redshifts of the objects and

lead to distortion of the apparent shape of the clusters in redshift space. The MTs can capture information on the shape of objects and hence can be used to measure the distortion of shape of the clusters. We discuss the effect of applying a linear redshift-space distortion operator on simulated density fields in three dimensions, which leads to a shift in the amplitude of the elements of the MTs. This shift in amplitude can be measured and used to constrain the redshift-space distortion parameter.

In chapter 6, we discuss noncommutative spacetime as predicted by some quantum theories of gravity and its effect on the angular power spectrum of the CMB temperature fluctuations and polarization fields. We find that this effect is dominant in the multipole range $\ell < 3000$ which is the range probed by *Planck* and hence *Planck* data is suitable to constrain spacetime noncommutativity. Further, we perform a bayesian analysis of the *Planck* 2013 temperature fluctuations data to obtain constraints on the energy scale at which spacetime noncommutativity becomes relevant. Our results improve upon the results of previous works by a factor of about two.

## 7.2 Future prospects

So far, there has been no strong observational evidence supporting the prediction of noncommutative spacetime. In our anaylsis of the CMB temperature fluctuations data provided by *Planck*, we found that the effect of spacetime noncommutativity on the CMB angular power spectrum is most prominent in the range of multipoles probed by *Planck*. Based on our analysis of this effect in the theoretical CMB angular power spectra produced by the CAMB package, we concluded that CMB data of higher resolutions would not significantly improve upon the constraints on the energy scale of spacetime noncommutativity. At the surface of last scattering, photons began to free stream and the diffusion of photons between regions having different temperatures lead to a dilution of the differences in temperatures between these regions. As a result, the information that can be extracted by probing smaller and smaller scales in the CMB fields, is limitted. However, a more detailed analysis of the effect of spacetime noncommutativity on the CMB power spectrum at smaller scales is necessary before we can claim that the constraints on the energy scale of noncommutativity can not be significantly improved by future data with higher resolutions. For this purpose, we can consider future cosmic variance limitted CMB experiments with higher angular resolutions than *Planck*. We can then forecast the constraint on the spacetime noncommutativity energy scale from such an experiment and compare the forecasted constraints to those obtained using *Planck* data. Such an analysis will enable us

to comment on whether or not CMB data with higher angular resolution can improve the constraint on the spacetime noncommutativity energy scale, and if yes, then how much of an improvement we can expect from such an experiment. This work would be important in providing guidance towards future searches for the noncommutativity of spacetime, which is a prediction of string theory and other quantum theories of gravity.

In their analysis of the SI of the CMB data from *Planck* using stereographic projections [30], the authors found no significant deviation from SI in the CMB temperature fluctuations data. However, they found $\approx 4$-$\sigma$ deviation from SI in the CMB polarization maps given in the *Planck* 2015 data release. It is important to test these results by direct computation of MTs on the sphere, before we search for physical explanations for the discrepancy. We have developed a method to compute MTs for random fields directly on the sphere and applied our method to the CMB temperature fluctuations data. We found excellent agreement between the data and the statistically isotropic $\Lambda$CDM simulations for the CMB temperature maps. As a next step, our method can be applied for computing the MTs on the sphere for the CMB polarization data and the results can be compared with those obtained from isotropic simulations. This work would shed light on the contribution of the stereographic projection to the 4-$\sigma$ deviation from isotropy in CMB polarization data found in [30]. If there is indeed a violation of SI in the CMB polarization, then it would require physical explanations regarding the origin of the anisotropy. Additionally, a detailed analysis of the *Planck* 30 GHz instrument beam and residual noise needs to be performed before we can conclude that the $\approx 2$-$\sigma$ discrepancy found in *Planck* 30 GHz temperature observations is of physical origin. This can be done by performing a MT analysis with varying smoothing angles of the *Planck* 30 GHz noise maps and simulated isotropic maps convolved with the *Planck* 30 GHz beam.

It is also interesting to study the statistical properties of the CMB foreground fields. Studying the properties of these fields could give important physical insights regarding the mechanisms that give rise to the respective emissions, as well as the distribution of matter in our galaxy. A better understanding of the foreground fields would also help in improving the accuracy of CMB extraction. In [119], the authors use skewness and kurtosis to test the Gaussianity of the Haslam 408 MHz map, which describes the synchrotron radiation from our galaxy. Surprisingly, they found that the statistical properties of the Haslam map are strongly Gaussian at the small scales. Investigating the origin of this property could yield important information about the distribution of free electrons in our galaxy.

# BIBLIOGRAPHY


[1] A. A. Penzias and R. W. Wilson, *Astrophys. J.*, **142***, 419* (1965) .

[2] R. Dicke et al., *Astrophys. J.*, **142***, 414-419* (1965) .

[3] A. A. Starobinsky, *Pis'ma Zh. Eksp. Teor. Fiz.* **30***, 719*, *[JETP Lett. 30, 682 (1979)]* (1979) .

[4] A. H. Guth, *Phys. Rev. D*, **23***, 347* (1981) .

[5] A. A. Starobinsky, *Phys. Lett. B*, **117***, 175* (1982) .

[6] A. D. Linde, *Phys. Lett. B*, **108***, 175* (1982) .

[7] A. Albrecht and P. J. Steinhardt, *Phys. Rev. Lett.*, **48***, 1220* (1982) .

[8] D. Fixsen et al., *Astrophys. J.*, ***473*** *576, [arXiv:astro-ph/9605054]* (1996) .

[9] G. F. Smoot et al., *Astrophys. J.*, **396** *L1* (1992) .

[10] T. J. Sodroski et al., *Astrophys. J.*, ***428*** *2 638* (1994) .

[11] C. L. Bennett et al., *Astrophys. J. Suppl. Ser.*, ***148*** *1* (2003) .

[12] C. L. Bennett et al., *Astrophys. J. Suppl. Ser.*, ***192*** *17* (2011) .

[13] R. Adam et al. [Planck Collaboration], *Astron. Astrophys.*, *594, A9* (2016) .

[14] J. Silk, *Astrophys. J.*, ***151*** *459* (1968) .

[15] Planck Images, "https://www.cosmos.esa.int/web/planck/."

[16] Peebles PJE, *Astrophys. J.*, *153:1–11* (1968) .

[17] Zel'dovich Y, Kurt V, Sunyaev R., *Sov. PHYS. -JETP*, *28:146* (1969) .

[18] E. Akofor, A. P. Balachandran, S. G. Jo, A. Joseph, and B. A. Qureshi, *J. High Energy Phys.*, *05 092* (2008) .

[19] E. Akofor, A. P. Balachandran, A. Joseph, L. Pekowsky and B. A. Qureshi, *Phys. Rev. D*, **79***, 063004* (2009) .

[20] Joby P. K., P. Chingangbam and S. Das, *Phys. Rev. D*, *91, 083503* (2015) .

[21] J. R. Bond, D. Pogosyan and T. Souradeep, *Phys. Rev. D*, *62, 043005* (2000) .

[22] T. Schücker, A. Tilquin and G. Valent, *MNRAS*, *444, Issue 3, 2820-2836* (2014) .

[23] M. E. Rodrigues et al., *Phys. Rev. D*, *86, 104059* (2012) .

[24] J. Soda, *Class. Quant. Grav.*, **29***, 083001 [arXiv:1201.6434 [hep-th]]* (2012) .

[25] K. Dimopoulos, *Int. Journal of Modern Phys. D*, *21, 03, 1250023* (2012) .

[26] A. Maleknejad et al., *Physics Reports*, *528, Issue 4, 161-261* (2013) .

[27] Razieh Emami, *arxiv:1511.01683*, *[astro-ph.CO]* (2015) .

[28] Tarun Souradeep, Amir Hajian, Soumen Basak, *New Astronomy Reviews*, *50 889-895* (2006) .

[29] Pranati K. Rath, Pramoda Kumar Samal, *Mod. Phys. Lett.*, *A30 1550131* (2015) .

[30] V. Ganesan and P. Chingangbam, *JCAP*, ***06*** *023, [arXiv:1608.07452] [INSPIRE]* (2017) .

[31] P. A. R. Ade et al. [Planck Collaboration], *Astron. Astrophys.*, *571, A15* (2014) .

[32] N. Padmanabhan, X. Xu, D. J. Eisenstein, R. Scalzo, A. J. Cuesta, et al., *Mon. Not. Roy. Astron. Soc.*, **427** *no. 3, 2132–2145, [arXiv:1202.0090 [astro-ph.CO]* (2012) .

[33] L. Anderson, E. Aubourg, S. Bailey, D. Bizyaev, M. Blanton, et al., *Mon. Not. Roy. Astron. Soc.*, **427** *no. 4, 3435–3467, [arXiv:1203.6594 [astro-ph.CO]* (2013) .

[34] F. Beutler, C. Blake, M. Colless, D. H. Jones, L. Staveley-Smith, et al., *Mon. Not. Roy. Astron. Soc.*, **416** *3017–3032, [arXiv:1106.3366 [astro-ph.CO]]* (2011) .

[35] P. A. R. Ade, et al. [BICEP2 Collaboration], *Phys. Rev. Lett.*, **112***, 241101 [arXiv:1403.3985 [astro-ph.CO]]* (2014) .

[36] K. M. Gorski et al., *Astrophys. J.*, *622, 759* (2005) .

[37] HEALPIX, "http://healpix.sourceforge.net."

[38] Planck Legacy Archive, "http://pla.esac.esa.int/pla/#maps."

[39] J. Cardoso et al., *Ieee Journal of Selected Topics in Signal Processing*, *2, 735* (2008) .

[40] Planck Collaboration XII., *Astron. Astrophys.*, *571, A12* (2014) .

[41] Eriksen, H. K., O'Dwyer, I. J., Jewell, J. B., et al., *ApJS*, *155, 227* (2004) .

[42] Eriksen, H. K., Jewell, J. B., Dickinson, C., et al., *ApJ*, *676, 10* (2008) .

[43] Basak, S., & Delabrouille, *J. MNRAS*, *419, 1163* (2012) .

[44] Basak, S., & Delabrouille, *J. MNRAS*, *435, 18* (2013) .

[45] Leach, S. M., Cardoso, J.-F., Baccigalupi, C., et al., *Astron. Astrophys.*, *491, 597* (2008) .

[46] Fernández-Cobos, R., Vielva, P., Barreiro, R. B., & Martínez-González, *MNRAS*, *420, 2162* (2012) .

[47] http://camb.info/.

[48] A. Lewis and S. Bridle, *Phys. Rev. D*, **66***, 103511 [astro-ph/0205436]* (2002) .

[49] http://cosmologist.info/cosmo/.

[50] J. Kovac et al., *Nature*, **420** *772 [astro-ph/0209478][INSPIRE]* (2002) .

[51] J.R. Bond and G. Efstathiou, *MNRAS*, **226** *655[IN SPIRE]* (1987) .

[52] R.J. Adler, *https://doi.org/10.1137/1.9780898718980*, .

[53] H. Tomita, *Prog. Theor. Phys.*, **76** *952* (1986) .

[54] J.R. Gott et al., *Astrophys. J.*, **352** *1* (1990) .

[55] K. R. Mecke, T. Buchert, and H. Wagner, *Astron. Astrophys.*, **288** *697* (1994) .

[56] J. Schmalzing and T. Buchert, *Astrophys. J.*, **482** *L1-L4* (1997) .

[57] J. Schmalzing and K.M. Gorski, *Mon. Not. Roy. Astron. Soc.*, ***297*** *355 [astro-ph/9710185][INSPIRE]* (1998) .

[58] S. Winitzki and A. Kosowsky, *New Astron.*, **3** *75* (1998) .

[59] T. Matsubara, *Astrophys. J.*, **584** *1* (2003) .

[60] T. Buchert, M. J. France and F. Steiner, *Class. Quantum Grav.*, **34***, 094002* (2017) .

[61] D. Novikov, J. Schmalzing and V. F. Mukhanov, *Astron. Astrophys.*, **364** *17* (2000) .

[62] E. Komatsu et al., *ApJS*, *192, 18* (2011) .

[63] V. Ganesan, P. Chingangbam, K.P. Yogendran and C. Park, *JCAP*, **02** *028* (2015) .

[64] P. A. R. Ade et al.[Planck Collaboration], *Astron. Astrophys.*, **594** *A17* (2016) .

[65] P. A. R. Ade et al.[Planck Collaboration], *Astron. Astrophys.*, **594** *A16* (2016) .

[66] P. Chingangbam and C. Park, *JCAP*, **02** *031* (2013) .

[67] D. Munshi, B. Hu, T. Matsubara, P. Coles and A. Heavens, *JCAP*, **04** *056* (2016) .

[68] L. Santos, K. Wang and W. Zhao, *JCAP*, **07** *029* (2016) .

[69] P. Coles and J. D. Barrow, *MNRAS*, **228** *407* (1987) .

[70] P. Chingangbam, C. Park, K. P. Yogendran and R. van de Weygaert, *Astrophys. J.*, **755** *122* (2012) .

[71] C. Park et al., *JKAS*, **46** *125* (2013) .

[72] D. Pogosyan, C. Gay and C. Pichon, *Phys. Rev. D*, **80** *081301* (2009) .

[73] P. McMullen, *Rend. Circ. Palermo*, **50** *259* (1997) .

[74] S. Alesker, *Geom. Dedicata*, **74** *241-248* (1999) .

[75] C. Beisbart, R. Dahlke, K. Mecke and H. Wagner, *Physics and Geometry of Spatially Complex Systems (ed. by K. Meche and D. Stoyan)*, *Vol. 600 of Lecture Notes in Physics pp. 249-271* (2002) .

[76] D. Hug, R. Schneider and R. Schuster, *Math. J.*, **19** *137-158* (2008) .

[77] G.E. Schroder-Turk, S. Kapfer, B. Breidenbach, C. Beisbart and K. Mecke, *J. Microsc.*, ***238*** *57* (2010) .

[78] G.E. Schroder-Turket al., *New J. Phys.*, **15** *083028* (2013) .

[79] A. Moor, *Acta Math.*, ***86*** *71* (1951) .

[80] W. Fabian, *Proc. Edinburg Math. Soc.*, ***10*** *145* (1957) .

[81] P. Chingangbam, K. P. Yogendran, Joby P. K., V. Ganesan, S. Appleby and C. Park, *JCAP*, ***12*** *023* (2017) .

[82] P.D. Naselsky and D.I. Novikov, *Astrophys. J*, ***507*** *31 [astro-ph/9801285][INSPIRE]* (1998) .

[83] E. A. Lim and D. Simon, *JCAP*, ***01*** *048 [arXiv:1103.4300][INSPIRE]* (2012) .

[84] Joby P. K., P. Chingangbam, T. Ghosh, V. Ganesan and Ravikumar C. D., *arxiv:1807.01306 [astro-ph.co]*, 2018.

[85] S. Appleby et al., *Astrophys. J.*, ***858*** *87* (2018) .

[86] J. Liske et al., *MNRAS*, ***452****, 2, 2087-2126* (2015) .

[87] K. S. Dawson et al., *AJ*, ***151****, 44* (2016) .

[88] K. Bundy et al., *Astrophys. J.*, ***798****, 7* (2015) .

[89] M. R. Blanton et al., *AJ*, ***154****, 28* (2017) .

[90] S. Appleby, P. Chingangbam, C. Park, K. P. Yogendran and Joby P. K., *Astrophys. J.*, ***863*** *200* (2018) .

[91] A. Doi and A. Koide, *IEICE Trans.*, ***E74*** *214* (1991) .

[92] C. S. Chu, B. R. Greene and G. Shiu, *Mod. Phys. Lett.*, *A16 2231-2240, [arXiv: hep-th/0011241]* (2001) .

[93] F. Lizzi, G. Mangano, G. Miele, M. Peloso, *Jhep*, *0206 049, [arXiv: hep-th/0203099]* (2002) .

[94] R. Brandenberger and P. M. Ho, *Phys. Rev. D*, **66***, 023517 [arXiv:hep-th/0203119]* (2002) .

[95] Q. G. Huang and M. Li, *Jhep 0306 (2003) 014, [arxiv:hep-th/0304203]*, *Q. G. Huang, M. Li, JCAP 0311 (2003) 001, [arXiv:astro-ph/0308458]* (2003) .

[96] S. Tsujikawa, R. Maartens and R. Brandenberger, *Phys. Lett. B*, *574 141-148 [arXiv:astro-ph/0308169]* (2003) .

[97] L. Barosi, F. A. Brito, A. R. Queiroz, *Jcap*, *0804:005 [arXiv:0801.0810[hep-th]]* (2008) .

[98] A. H. Fatollahi, M. Hajirahimi, *Europhys. Lett.*, *75 542-547, [arXiv:astro-ph/0607257]* (2006) .

[99] A. H. Fatollahi, M. Hajirahimi, *Phys. Lett. B*, *641 381-385, [arXiv:hep-th/0611225]* (2006) .

[100] S. Fabi, B. Harms and A. Stern, *Phys. Lett. D*, **78***, 065037, [arXiv:0808.0943 [hep-th]]* (2008) .

[101] K. Karwan, *Eur. Phys. J. C*, *521 [arXiv:0903.2806 [astro-ph.CO]]* (2010) .

[102] Y. Shtanov and H. Pyatkovska, *Phys. Rev. D*, **80***, 023521 (2009), [Erratum-ibid. D* **83***, 069904] [arXiv:0904.1887 [gr-qc]]* (2011) .

[103] B. Malekolkalami and M. Farhoudi, *Class. Quant. Grav.*, **27***, 245009 [arXiv:1007.2499 [gr-qc]]* (2010) .

[104] M. Moumni, A. BenSlama and S. Zaim, *J. Geom. Phys.*, **61***, 151 [arXiv:0907.1904 [hep-ph]]* (2011) .

[105] T. S. Koivisto and D. F. Mota, *Jhep*, **1102***, 061 [arXiv:1011.2126 [astro-ph.CO]]* (2011) .

[106] A. Nautiyal, *Phys. Lett. B*, **728** *472 [arXiv:1303.4159 [astro-ph.CO]]* (2014) .

[107] E. Komatsu et al., *J. Suppl. Ser.*, *180, 330* (2009) .

[108] M. R. Nolta et al., *Astrophys. J. Suppl. Ser.*, *180, 296* (2009) .

[109] J. Dunkley et al., *Astrophys. J. Suppl. Ser.*, *180, 306* (2009) .

[110] C. L. Reichardt et al., *ApJ*, *694, 1200* (2009) .

[111] C. L. Kuo et al., *ApJ*, *664, 687* (2007) .

[112] C. L. Kuo et al., *ApJ*, *600, 32* (2004) .

[113] B. S. Mason et al., *ApJ*, *591, 540* (2003) .

[114] J. L. Sievers et al., *ApJ*, *660, 976* (2007) .

[115] J. L. Sievers et al., *ApJ*, *591, 599* (2003) .

[116] T. J. Pearson et al., *ApJ*, *591, 556* (2003) .

[117] A. C. S. Readhead et al., *ApJ*, *609, 498* (2004) .

[118] M. Shiraishi, D. F. Mota, A. Ricciardone and F. Arroja, *Jcap*, **1407***, 047 [arXiv:1401.7936 [astro-ph.CO]]* (2014) .

[119] A. Ben-David, S. V. Hausegger and A. D. Jackson, *JCAP*, *11 019* (2015) .